

PREDICTION OF THERMAL CONTACT CONDUCTANCE BY
STATISTICAL MECHANICS

BY

MICHAEL LEUNG

A DISSERTATION PRESENTED TO THE GRADUATE SCHOOL OF THE
UNIVERSITY OF FLORIDA IN PARTIAL FULFILLMENT OF THE
REQUIREMENTS FOR THE DEGREE OF DOCTOR OF PHILOSOPHY

UNIVERSITY OF FLORIDA

1995

To my family

ACKNOWLEDGEMENTS

I would like to acknowledge those individuals whose assistance made this dissertation possible.

Dr. C.K. Hsieh, chairman of the committee, selflessly devoted his time to provide guidance and encouragement during the course of the research. I also learned enormously in his graduate courses. It is a great pleasure to have an opportunity to be both his advisee and his student.

I would like to thank Dr. D.Y. Goswami, cochairman of the committee, for his advice and patience. In addition, I am grateful to him for offering me opportunities to participate in his projects that broaden my research background.

I would like to extend my sincere appreciation to the committee members Drs. J.F. Klausner, U.H. Kurzweg, and E.D. Whitney for the time, direction, and knowledge that they put forth toward the completion of the research.

A number of technical supports were put together to make the experiment possible. Dr. Y. Takano, Associate Professor of Physics, and Mr. S. Miyamoto, graduate student, are greatly appreciated for allowing me to use the nano-voltmeter in their laboratory. I would also like to thank Dr. M.J. Kaufman, Associate Professor, and Dr. P.H. Holloway, Professor of Materials Science, for letting me measure the microhardness and surface

profiles with their instruments. Special thanks go to Mr. C. Garretson, senior engineering technician, for assisting in apparatus and specimen preparation.

Finally, I would like to express my gratitude to my family for their unconditional love and support throughout my collegiate career. Without any of the above assistance, it would have been much more difficult to complete my Ph.D. degree.

TABLE OF CONTENTS

	<u>page</u>
ACKNOWLEDGEMENTS	iii
LIST OF TABLES	vii
LIST OF FIGURES	viii
NOMENCLATURE	xi
ABSTRACT	xiii
CHAPTERS	
1 INTRODUCTION	1
2 MECHANISMS OF THERMAL CONTACT CONDUCTANCE	3
2.1 Conduction through True Contact Areas	6
2.2 Thermal Radiation	6
2.3 Convection and Conduction through Interstitial Medium	7
3 LITERATURE REVIEW	10
3.1 Review Papers	10
3.2 Theoretical Models	11
3.2.1 Constriction Resistance due to Single Contact	13
3.2.2 Hsieh Model	18
3.2.3 Yovanovich Model	22
3.2.4 Modified Greenwood and Williamson Model	24
3.3 Experimental Studies	28
3.3.1 Experimental Setup	28
3.3.2 Sources of Experimental Data	30
4 THEORETICAL BASIS FOR THE USE OF STATISTICAL MECHANICS ...	32
4.1 Microscopic and Macroscopic Points of View of Contact Conductance	32

4.2	Boltzmann Statistics and Thermodynamics	33
4.3	Comparison between Contact Conductance and Statistical Thermodynamics	37
5	MOST PROBABLE DISTRIBUTION OF SUMMIT HEIGHTS BY BOLTZMANN STATISTICAL MODEL	39
5.1	Surface Measurement as Constraints	39
5.2	Derivation by Boltzmann Statistical Model	42
6	PREDICTION OF THERMAL CONTACT CONDUCTANCE BY BOLTZMANN STATISTICAL MODEL	50
6.1	Development of Core Equations	51
6.2	Plastic Cone Model	57
6.3	Plastic Cone and Elastic Base Model	66
6.4	Elastic Spherical Asperity Model	70
6.5	Elastic and Plastic Spherical Asperity Model	76
7	NUMERICAL RESULTS AND DISCUSSION	80
7.1	Numerical Method	80
7.2	Numerical Data	81
7.3	Discussion	100
8	MEASUREMENT OF ELECTRICAL CONTACT CONDUCTANCE	108
8.1	Surface Preparation and Measurement	109
8.2	Apparatus Setup and Data Collection	110
8.3	Empirical Results and Discussion	117
9	CONCLUSIONS AND RECOMMENDATIONS	123
REFERENCES	126
APPENDIXES		
A	MATHEMATICAL EQUATIONS	130
B	RECORDED SURFACE PROFILES	131
BIOGRAPHICAL SKETCH	136

LIST OF TABLES

<u>Table</u>	<u>page</u>
3.1 Summary of constriction alleviation factors obtained by Gibson, Roess, and Cooper et al.	19
4.1 Similarities between the domain of statistical thermodynamics and that of thermal contact conductance	38
7.1 Experiments for thermal contact conductance of nominally-flat surfaces in a vacuum environment	82
8.1 Summary of surface roughness	111

LIST OF FIGURES

<u>Figure</u>	<u>page</u>
2.1 Illustration of thermal contact conductance: a) heat flows through two bodies in contact and b) the corresponding temperature profile	4
2.2 Convergence of heat flow from a semi-infinite medium to discrete contact spots	5
2.3 Natural convection between hot and cold parallel walls in three different extreme cases	8
3.1 Estimation of the number and sizes of contact spots by a graphical means	12
3.2 Heat flows through a single constriction in a semi-infinite medium	14
3.3 Heat flows across two semi-infinite media through a single constriction	16
3.4 Cylindrical flow channel and the corresponding boundary conditions	17
3.5 Surface roughness modeled by conical asperities	20
3.6 Asperity deformation mechanism used by the Hsieh model	21
3.7 a) Contacting rough surfaces modeled by b) the contact between a flat and an equivalent rough surface	23
3.8 Surface roughness modeled by spherical asperities	26
3.9 Schematic of experimental test facility	29
5.1 Distributions of surface heights and summit heights of a bead-blasted surface	41
6.1 Demonstration of modeling technique used in contact area formation	52
6.2 Plastic deformation at asperity summits	59
6.3 Illustration of penetration depth for non-contacting asperities	64

6.4	Illustration of plastic summit and elastic base deformation	67
6.5	Material deformation between spherical asperities	73
7.1	Thermal contact conductance versus contact pressure for Stainless Steel 303 surfaces in a vacuum (Data 1)	83
7.2	Thermal contact conductance versus contact pressure for Stainless Steel 303 surfaces in a vacuum (Data 2)	84
7.3	Thermal contact conductance versus contact pressure for Stainless Steel 416 surfaces in a vacuum (Data 3)	85
7.4	Thermal contact conductance versus contact pressure for Nickel 200 surfaces in a vacuum (Data 4)	86
7.5	Thermal contact conductance versus contact pressure for Nickel 200 surfaces in a vacuum (Data 5)	87
7.6	Thermal contact conductance versus contact pressure for Stainless Steel 304 surfaces in a vacuum (Data 6)	88
7.7	Thermal contact conductance versus contact pressure for Stainless Steel 304 surfaces in a vacuum (Data 7)	89
7.8	Thermal contact conductance versus contact pressure for Zirconium-2.5%wt Nb surfaces in a vacuum (Data 8)	90
7.9	Thermal contact conductance versus contact pressure for Zirconium-2.5%wt Nb surfaces in a vacuum (Data 9)	91
7.10	Thermal contact conductance versus contact pressure for Zircaloy-4 surfaces in a vacuum (Data 10)	92
7.11	Thermal contact conductance versus contact pressure for Zircaloy-4 surfaces in a vacuum (Data 11)	93
7.12	Thermal contact conductance versus contact pressure for Aluminum 6061-T6 surfaces in a vacuum (Data 12)	95
7.13	Thermal contact conductance versus contact pressure for Stainless Steel 304 surfaces in a vacuum (Data 13)	96

7.14 Thermal contact conductance versus contact pressure for Stainless Steel 304 surfaces in a vacuum (Data 14)	97
7.15 Thermal contact conductance versus contact pressure for Stainless Steel 304 surfaces in a vacuum (Data 15)	98
7.16 Dimensionless thermal contact conductance versus dimensionless contact pressure	99
7.17 Thermal contact conductance versus contact pressure for a) Data 5 and b) Data 6	101
7.18 Illustration of the difference in deformation of asperities for a given contact pressure between a) the plastic cone model and b) the plastic cone and elastic base model	104
7.19 Stress-strain analyses used by the two spherical asperity models: a) elastic model and b) elastic and plastic model	106
8.1 Schematic of electrical conductivity measurement	112
8.2 Connection of an electrode to a specimen	113
8.3 Measured resistance of stainless steel bar stock versus length	114
8.4 Schematic of the apparatus for testing electrical contact conductance	116
8.5 Electrical contact conductance versus contact pressure for Stainless Steel 304 surfaces (Set 1)	118
8.6 Electrical contact conductance versus contact pressure for Stainless Steel 304 surfaces (Set 2)	119
8.7 Demonstration of larger pure metal-metal contact area produced by a) rough surfaces in contact than by b) smoother surfaces in contact	122
B.1 Recorded surface profiles of Specimen A: a) 0° and b) 90°	132
B.2 Recorded surface profiles of Specimen B: a) 0° and b) 90°	133
B.3 Recorded surface profiles of Specimen C: a) 0° and b) 90°	134
B.4 Recorded surface profiles of Specimen D: a) 0° and b) 90°	135

NOMENCLATURE

A	area
a	circular contact spot radius
b	radius of cylindrical heat flow channel
C_i	constants
D_{zero}	density of zeroes (number per unit length)
D_{ext}	density of extrema (number per unit length)
d	mean plane separation
E	Modulus of Elasticity
F	loading force on a contact spot
$f(z)$	probability density function of property z
g_{gra}	gravity
g	statistical weight
H	microhardness
h	thermal/electrical contact conductance
I	electrical current
k	thermal/electrical conductivity
k_B	Boltzmann constant
L	length
m	slope
m_{oi}	i-th moment of power spectral density
N_j	number of particles or asperities having property j
N	total number of particles or asperities
$P(z)$	probability of occurrence z
P	applied pressure
p_0	maximum Hertzian pressure
q	heat rate
q''	heat flux
R	mean radius of asperity summits
R_c	constriction resistance
R_e	electrical resistance
R_{TOT}	total resistance
Ra_L	Rayleigh number
S	shift of distribution curve
T	temperature
U	total internal energy of an enclosed system
u_j	energy corresponding to energy level j
V	electrical voltage
w	thermodynamic probability (number of ways that a given distribution can arise)
x	height (asperity or surface)

Greek Letters

α_{th}	thermal diffusivity
β_{th}	coefficient of volumetric thermal expansion
α, β, γ	Lagrange multipliers
δ	asperity summit penetration depth
ξ	base plane separation
ϵ	emissivity
σ_{SB}	Stefan-Boltzmann constant
ν_f	kinematic viscosity of fluid
ν	Poisson ratio
σ	standard deviation
μ	mean
ρ	bandwidth parameter
Ψ	constriction alleviation factor
$\phi(z)$	probability density function of a Gaussian distribution of z
ζ, κ, τ	lumped parameters
λ	empirical factor

Abstract of Dissertation Presented to the Graduate School of the University of Florida
in Partial Fulfillment of the Requirements for the Degree of Doctor of Philosophy

PREDICTION OF THERMAL CONTACT CONDUCTANCE BY
STATISTICAL MECHANICS

By

Michael Leung

August, 1995

Chairman: C.K. Hsieh

Cochairman: D.Y. Goswami

Major Department: Mechanical Engineering

Despite the substantial theoretical studies of thermal contact conductance in the past decades, the application of statistical mechanics in this field has never been considered. The Boltzmann statistical model is attempted in this study to predict the distribution of true contact spots between two metal surfaces on which asperities are distributed homogeneously and isotropically. Further, the relationship between the thermal contact conductance and the relative interfacial pressure is derived. Different assumptions of surface asperity deformation mechanisms lead to the development of four theoretical models. Among them, the most effective model is the plastic cone model, in which surface roughness is resembled by conical asperities and the load-carrying asperities are deformed plastically. The numerical results are compared to a wide range of published empirical data and a good order-of-magnitude agreement is found.

In this study, the conventional assumption of Gaussian summit heights is shown to be unnecessary. The probability density function of this kind is determined naturally by means of the Boltzmann model.

Experiments were also conducted in order to verify the accuracy of the predictions by the Boltzmann model. Electrical contact conductance, simulating the thermal contact conductance effect in a vacuum environment, was measured. The tested surfaces were made of Stainless Steel 304 and finished by sandblasting. The experimental results indicate the presence of electrically insulating surface films. The correction factors applied to the predictions are of the magnitude reported in the previous studies.

CHAPTER 1

INTRODUCTION

When two solid bodies at different temperatures are brought into mechanical contact, a relatively high thermal resistance impedes the heat flow across the interface. This resistance, commonly known as thermal contact resistance, arises because the heat-flow path is lengthened as a result of the actual contact area being only a small fraction of the apparent contact area. Sometimes, the thermal contact resistance is expressed in its reciprocal form, called thermal contact conductance.

Engineers often encounter contact conductance in a wide range of thermal systems, including advanced storage electric water heaters [1], nuclear reactors [2], high-power density space vehicles [3], among others. Recently, thermal contact conductance has been found to play an important role in small-scale heat removal systems such as microelectronics [4] and in heat transfer between superconductor films and substrates [5]. Thus, the contact conductance has received renewed interest and attention.

Due to the considerable effect of the contact conductance, many theoretical and experimental investigations have been performed in the last five decades. Significant advances have been made in the development of theoretical models to predict the contact conductance. In the experimental arena, efforts have been made in the use of contact

conductance for thermal rectification [6,7] and in the use of metallic coatings to enhance contact conductance [8,9].

Among all the existing theoretical models, the use of statistical mechanics has never been attempted even though it is a potentially promising approach. The physical foundation is based on the surface asperities comparable to molecules in the traditional sense of microscopic viewpoint. The focus of this investigation is thus directed toward the application of statistical mechanics to the prediction of contact conductance. Four different statistical mechanics-based models are developed. In each case, assumptions and detailed derivation are given. Numerical results show that the predicted conductance agrees reasonably well with a wide range of published empirical data. It is thus concluded that statistical mechanics is a feasible approach.

The electrical contact conductance between two stainless steel surfaces was tested. Due to the presence of surface films, the measured conductance is substantially lower than the prediction. The role of surface films in contact conductance is discussed in this dissertation.

CHAPTER 2

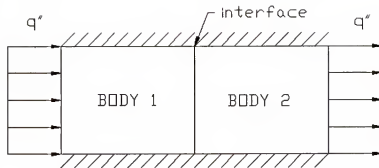
MECHANISMS OF THERMAL CONTACT CONDUCTANCE

The thermal contact conductance effect is illustrated in Fig. 2.1. When heat flows steadily across the joint of two solid bodies in mechanical contact, the temperature drops at the interface. This phenomenon is well-explained by the fact that the actual contact area is exceedingly small as compared to the apparent contact area due to the presence of roughness and waviness of the engaging surfaces. Moreover, the interstitial material, such as air, is a poor conductor. A large portion of the heat flow thus converges to the discrete solid-solid contact spots as illustrated in Fig. 2.2. The increase of the heat-flow path length results in a thermal resistance across the interface. Its reciprocal is the thermal contact conductance, defined as

$$h = \frac{q}{A \Delta T} \quad (2.1)$$

There are three possible modes of heat transfer at the interface. They are described in the sections that follow.

a)



b)

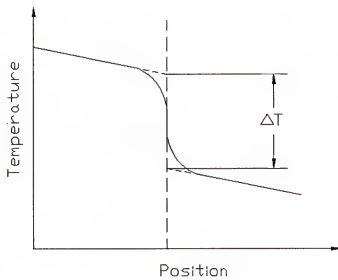


Fig. 2.1 Illustration of thermal contact conductance: a) heat flows through two bodies in contact and b) the corresponding temperature profile

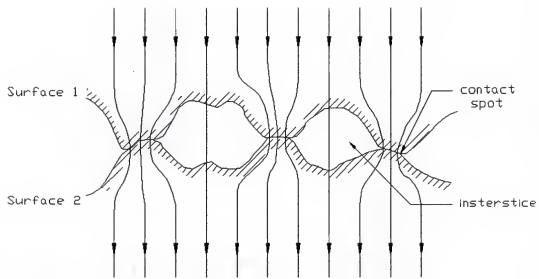


Fig. 2.2 Convergence of heat flow from a semi-infinite medium to discrete contact spots

2.1 Conduction through True Contact Areas

In most engineering applications, heat conduction through the actual contact spots is the dominant mode of heat transfer. Parameters directly involved in the thermal analysis of this heat transfer consist of the solid thermal conductivities and the distribution of the true contact spots. The formation of contact spots between two rough surfaces pressed together is thus the focus of this investigation of contact conductance. This mode of heat transfer will be elaborated on further in the literature review in Chapter 3.

2.2 Thermal Radiation

Heat can also travel by other means. For the portions of the surfaces which are not in physical contact, thermal radiation exchange can take place. This mode of heat transfer can be modeled by radiation exchange between two parallel walls and the relationship between the heat flux and the surface temperatures is expressed by

$$q'' = \frac{\sigma_{SB}(T_1^4 - T_2^4)}{1/\epsilon_1 + 1/\epsilon_2 - 1} \quad (2.2)$$

where σ_{SB} = Stefan-Boltzmann constant
 ϵ_i = emissivity of wall i , $i = 1, 2$

Unless the temperature difference at the interface is large, $(T_1 - T_2) >> 0$, the radiation contribution to the contact conductance is negligible for most practical applications. Fenech and Rohsenow show that the ratio of radiation to conduction through contact spots does not exceed 1 % when the interface is at a mean temperature as high as 600 °C [10].

2.3 Convection and Conduction through Interstitial Medium

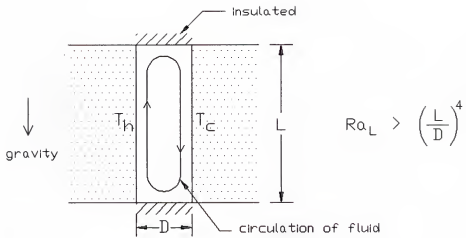
When the interstice is filled with a fluid, such as air, heat may be transferred by convection and conduction in the interstitial medium. The amount of convective heat transfer can be estimated again by a two lateral wall model. As Bejan [11] describes, the existence of the naturally driven fluid circulation between the hot and the cold walls can be tested by the Rayleigh number, which is expressed by

$$Ra_L = \frac{g_{\text{gra}} \beta_{\text{th}} (T_h - T_c) L^3}{\alpha_{\text{th}} \nu_f} \quad (2.3)$$

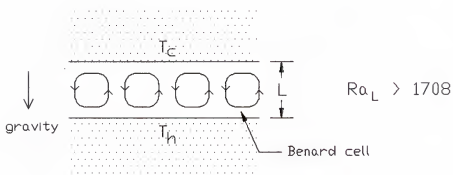
where
 g_{gra} = gravitational acceleration
 β_{th} = coefficient of volumetric thermal expansion
 α_{th} = thermal diffusivity
 ν_f = kinematic viscosity

For the case where a pair of vertical planes are evenly separated as illustrated in Fig. 2.3a, the critical condition of fluid motion is $Ra_L > (L/D)^4$. When the two walls are horizontally positioned, the critical condition becomes different as illustrated in Figs. 2.3b

a)



b)



c)

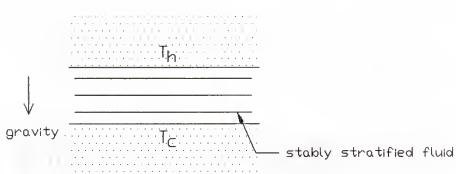


Fig. 2.3 Natural convection between hot and cold parallel walls in three different extreme cases

and 3c. For this system heated from below as shown in Fig. 2.3b, a Bénard convection flow pattern is induced when $\text{Ra}_L > 1708$. Conversely, for the system heated from the upper surface as shown in Fig. 2.3c, the gap is filled with quiescent, thermally stratified fluid and thus convection does not play a role.

For the interstitial fluid between nominally flat surfaces in mechanical contact, the above critical conditions are seldom satisfied because of the small gap thickness, of the order of $1 \mu\text{m}$. Therefore, the interstice is filled with quiescent fluid. Hence, heat transfer by natural convection does not occur.

The gap thickness is still orders of magnitude greater than the mean free path of gas molecules. For instance, the mean free path of oxygen at standard conditions is $8 \times 10^{-2} \mu\text{m}$ [12]. For this reason, the heat transfer through the interstitial material is entirely ruled by conduction under Fourier's law. In most experimental tests, this mode of heat transfer is commonly eliminated by measuring the thermal contact conductance in a vacuum environment.

CHAPTER 3 LITERATURE REVIEW

3.1 Review Papers

The bibliography by Hsieh and Davis listed most of the early publications dealing with the thermal contact resistance [13]. Subsequently, a number of other reviews have appeared in the literature which summarized a diverse range of related research performed more recently. Snaith et al. [14] presented a paper that was specifically aimed at assisting designers in understanding the physical factors involved by an overview of the literature in the areas of contact conductance. The mechanisms of heat transfer across a metal-metal interface and the analytical prediction methods were well presented. Other discussions in the review included parametric effects and empirical correlations.

Madhusudana and Fletcher summarized the work primarily completed in the 1970s [15]. They reviewed theoretical and experimental investigations dealing only with the heat transfer through the actual contact spots and the interstitial materials by conduction. Theoretical, numerical, and experimental analyses for constrictions of different shapes were considered and summarized in a table. Correlations of experimental data and some special topics including stacks of lamination, bolted joints, cylindrical joints, and nuclear reactor fuel elements were also covered.

A more recent review, again by Fletcher, surveyed the literature published since 1980 [16]. In addition to the primary areas described earlier, contact conductance in microelectronics and biomedicine, thermal rectification effect, gas conductance, and periodic and sliding contacts were also considered.

3.2 Theoretical Models

As mentioned before, the heat transfer across contacting surfaces in vacuum is mainly dominated by conduction through the discrete contact spots. The total resistance can thus be represented by all spot resistances, also known as the constriction resistances, in a parallel connection as

$$\frac{1}{R_{tot}} = \sum_i \frac{1}{R_{c,i}} \quad (3.1)$$

To make this expression useful, each constriction resistance, $R_{c,i}$, and the overall distribution of the true contacts must be available. Analytical solutions of the constriction resistance have been successfully developed and validated by a number of investigators. The details will be given shortly.

The distribution of contact spots, another important piece of information needed, can be obtained graphically by superposing two recorded profilometric traces as shown in Fig. 3.1 [10]. The number of contacts are then counted and the size of each contact is

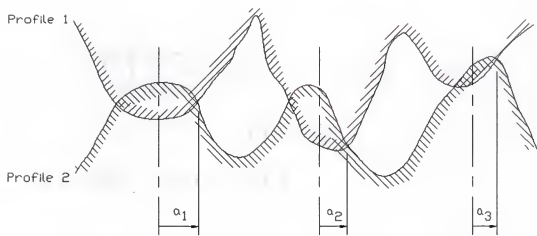


Fig. 3.1 Estimation of the number and sizes of contact spots by a graphical means

measured. In spite of the feasibility, the process is extremely laborious and time-consuming. Preference is thus given to mathematical modeling.

Three successful models developed in the past will be discussed in this section to illustrate the different features that have been considered previously. Some of these features, including the surface models and deformation mechanisms, are applied in conjunction with Boltzmann statistics to devise an approach to predict the thermal contact conductance. All these previous models apply to contact between nominally flat surfaces, so that the waviness effect is ignored. Their results will be presented along with the predictions obtained by the Boltzmann statistical model in Chapter 7 for comparison.

3.2.1 Constriction Resistance due to Single Contact

The closed form solution to the electrical resistance due to a single circular contact spot traces back to Holm [17] who used it to predict the electrical contact resistance. Under the condition where heat transfer by radiation, convection, and conduction through the interstitial materials is insignificant, the thermal resistance, heat rate, and temperature gradient are directly analogous to the electrical resistance, current, and potential gradient, respectively. Therefore, it is justified to apply Holm's work to the study of thermal contact conductance.

Holm's constriction resistance can be derived by using a Laplace equation in a semi-infinite medium of constant properties with the boundary conditions given in Fig. 3.2.

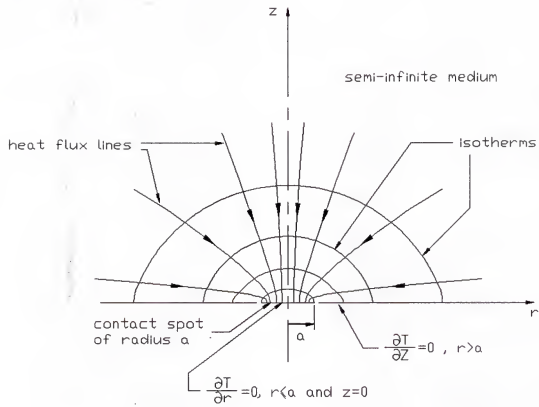


Fig. 3.2 Heat flows through a single constriction in a semi-infinite medium

The resultant resistance is obtained as

$$R_c = \frac{1}{4ak} \quad (3.2)$$

When the resistance is across two semi-infinite media of different materials, as illustrated in Fig. 3.3, the contact surfaces may be considered isothermal. Then, the total resistance can be represented as a sum as

$$R_c = \frac{1}{4ak_1} + \frac{1}{4ak_2} \quad (3.3)$$

For similar materials,

$$k_1 = k_2 = k$$

thus,

$$R_c = \frac{1}{2ak} \quad (3.4)$$

The above model provides accurate results when the actual area of contact is only a small fraction of the apparent area. As this fraction increases, heat traveling through a contact spot from a semi-infinite cylindrical medium becomes more realistic in analyzing the heat transfer. Figure 3.4 shows the schematic of this cylindrical heat channel, including the boundary conditions. The analytical solution to this system leads to a correction of Eq. 3.4 by a multiplying factor, namely, the constriction alleviation factor, Ψ , as

$$R_c = \frac{\Psi}{2ak} \quad (3.5)$$

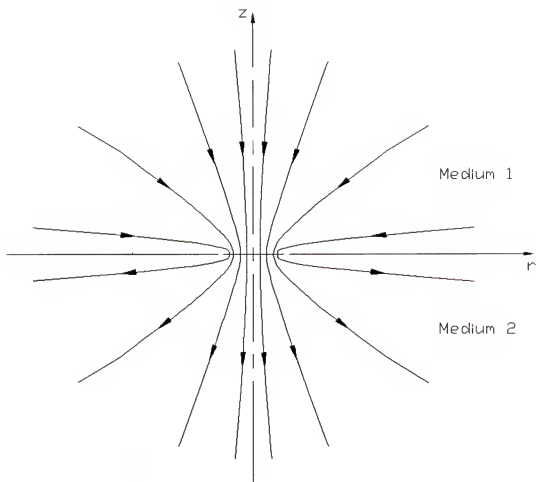


Fig. 3.3 Heat flows across two semi-infinite media through a single constriction

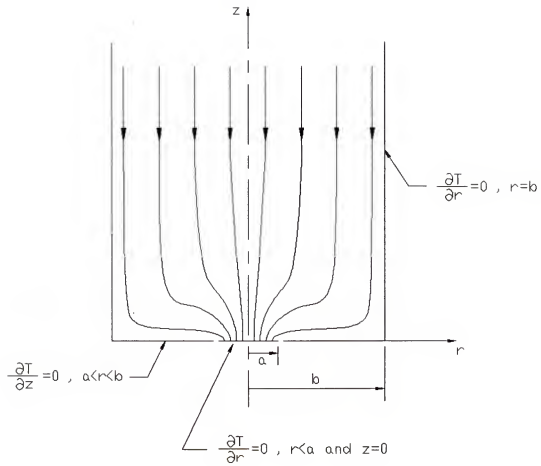


Fig. 3.4 Cylindrical flow channel and the corresponding boundary conditions

A number of investigators have successfully derived analytical and approximate solutions to this model. Gibson reduced the mixed boundary value problem to a Fredholm integral equation and then solved it [18]. A similar expression was obtained by Roess as presented by Snaith et al. [14]. Approximations given by Cooper et al. [19] were rather simple to use. All results mentioned above are summarized in Table 3.1.

3.2.2 Hsieh Model

Incorporating the constriction resistance analysis given above, Hsieh performed a statistical analysis to predict the total contact conductance [20]. His model is constructed on the basis of contact between a pair of homogeneous and isotropic surfaces. The irregularities of each rough surface are modeled by conical asperities of an identical gradient and various heights resting on a common flat plane; see Fig. 3.5. This surface model has been proven to be a suitable representation of the surfaces processed by grinding, lapping, honing, bead-blasting, anodizing, and accurate casting [21,22]. In addition, the summit height distribution is assumed Gaussian.

From the mechanical deformation point of view, touching asperities resemble blunt indenters. This results in a plastic summit deformation and a local elastic substrate deformation as shown in Fig. 3.6. Working collectively, they serve well to estimate the load distribution over the apparent area.

By using the above assumptions and a given base plane separation which is small enough to initiate contact, the probability density of surface asperities making contacts is

Table 3.1 Summary of constriction alleviation factors obtained by Gibson, Roess, and Cooper et al.

Gibson [18]	$\Psi = 1 - 1.4091839(a/b) + 0.338010(a/b)^3 + 0.067902(a/b)^5 + O((a/b)^6)$
Roess [14]	$\Psi = 1 - 1.40925(a/b) + 0.29591(a/b)^3 + 0.0525419(a/b)^5 + O((a/b)^6)$
Cooper et al. [19]	$\Psi = \begin{cases} (1 - a/b)^{1.5} & , \text{ all } a/b \\ 1 - 1.4(a/b) & , a/b \leq 0.5 \\ 1 & , \text{ small } a/b \end{cases}$

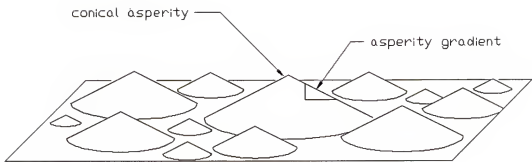


Fig. 3.5 Surface roughness modeled by conical asperities

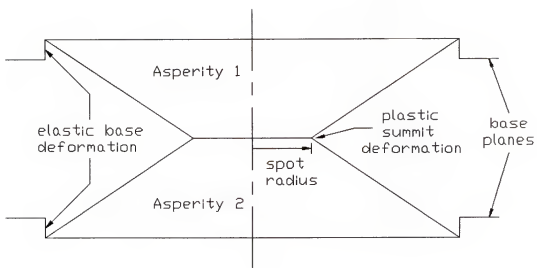


Fig. 3.6 Asperity deformation mechanism used by the Hsieh model [20]

derived. Knowing this probability density function, Hsieh finally evaluated the "expectations" of the total thermal contact conductance and the relative total load.

3.2.3 Yovanovich Model

In the past, a number of correlations have been proposed. The Yovanovich thermal contact model is one of the successful examples. This model was first presented by Cooper et al. [19] and later refined by Yovanovich [23]. Unlike the Hsieh model, it is assumed that the surface heights (not summit heights) form a Gaussian distribution. Moreover, the mean surface profile slope m is independent of the surface height. The contact between two rough surfaces is interpreted by a contact between a perfectly flat surface and an equivalent rough surface having combined surface parameters as illustrated in Fig. 3.7. These parameters lead to a combined RMS roughness, defined as

$$\sigma = \sqrt{\sigma_1^2 + \sigma_2^2} \quad (3.6)$$

and a combined mean slope, defined as

$$m = \sqrt{m_1^2 + m_2^2} \quad (3.7)$$

When two surfaces are pressing together, it is assumed that the summits of all contacting asperities are deformed plastically while the entire substrate undergoes an

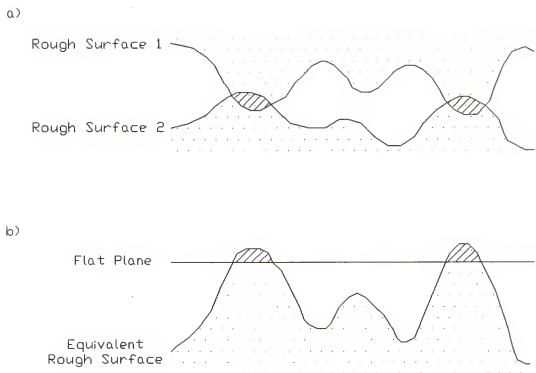


Fig. 3.7 a) Contacting rough surfaces modeled by b) the contact between a flat plane and an equivalent rough surface

elastic deformation (absence of local substrate deformation). By coupling this deformation mechanism with the surface statistical properties and the constriction resistance equation (Eq. 3.4), an expression giving a relationship among the contact conductance, the contact pressure, and other parameters involved can be derived. This expression is then correlated by a simple equation as

$$\frac{h \sigma}{km} = 1.25 \left(\frac{P}{H} \right)^{0.95} \quad (3.8)$$

where H and k are the harmonic mean hardness and conductivity, respectively. If the surfaces in contact are made of dissimilar materials,

$$\frac{1}{H} = \frac{1}{2} \left(\frac{1}{H_1} + \frac{1}{H_2} \right)$$

and

$$\frac{1}{k} = \frac{1}{2} \left(\frac{1}{k_1} + \frac{1}{k_2} \right)$$

Due to its accuracy and simplicity, the Yovanovich model is widely accepted and utilized.

3.2.4 Modified Greenwood-Williamson Model

With the belief that both plastic and elastic deformations of the contact asperities take place in practice, McWaid and Marschall [24] investigated an elastic contact model.

Known as the modified Greenwood-Williamson model, the method owes its origin to the work initially performed by Greenwood and Williamson [25].

The assumptions made here are quite different from the ones described previously. Since the summit of an asperity is commonly round, a rough surface is postulated as a flat plane covered with spherical asperities of an identical mean curvature as shown in Fig. 3.8. The fundamental surface parameters are the zeroth, second, and fourth moments of the power spectral density, denoted by m_0 , m_2 , and m_4 , respectively. Several topographic parameters, such as the standard deviation of the summit height, the density of summits, etc., can be expressed in terms of these spectral moments.

The estimation of the degree of engagement of the contact is treated in a similar fashion as Yovanovich. The contact between two rough surfaces is represented by the contact between an ideally smooth plane and an equivalent rough surface whose spectral moments equal to the sum of the respective moments of the individual surfaces. Additionally, this model assumes that the summit heights of the equivalent rough surface form a Gaussian distribution. The elastic deformation analysis of a single contact is accomplished by invoking the use of the Hertzian theory for the contact between a sphere and a plane [26].

Using the assumptions and analyses given above, one can obtain the expressions of the loading pressure P and the conductance h in terms of the mean plane separation d as

$$P = \frac{E \cdot (\rho - 0.8968)^{3/4} m_2^{1/2}}{30.03} \int_{d/\sigma}^{\infty} (x - d/\sigma)^{3/2} \phi(x) dx \quad (3.9)$$

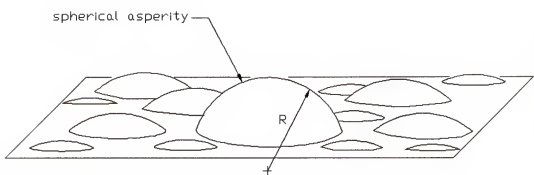


Fig. 3.8 Surface roughness modeled by spherical asperities

and

$$h = \frac{0.0375 km_4}{\psi mo_2} \left(\frac{\pi mo_0}{mo_4} \right)^{1/4} \left(1 - \frac{0.8968}{\rho} \right)^{1/4} \int_{d/\sigma}^{\infty} (x - d/\sigma)^{1/2} \phi(x) dx \quad (3.10)$$

where

$$E^* = \left(\frac{1 - v_1^2}{E_1} + \frac{1 - v_2^2}{E_2} \right)^{-1}$$

and

$$\rho = \frac{mo_0 mo_4}{mo_2^2}$$

Hence, a relationship between h and P is established.

McWaid and Marschall assume that all contacts undergo an elastic deformation. On the other hand, Tabor suggests a criterion for the onset of plastic deformation of a spherical asperity [27]. It is shown that the first plastic flow occurs when the maximum Hertzian pressure is greater than 60% of the indentation hardness. In other words, if the maximum pressure is less than that, the entire asperity is deformed elastically. Both mechanisms of deformation of the spherical asperities will be employed in conjunction with the Boltzmann statistical model in analyzing the contact conductance in Chapter 6. More details of this modeling technique, including the topographic parameters and the use of the Hertzian theory, will be discussed then.

3.3 Experimental Studies

3.3.1 Experimental Setup

In addition to the theoretical studies, numerous efforts have been made to measure the contact conductance experimentally. Mainly for the purpose of validating analytical models, the experimental measurements are indispensable in assessing the effects of the contacting materials, the interstitial fluids, or other characteristics of the surface on the contact conductance.

The schematic of an apparatus setup that appears repeatedly in the literature is shown in Fig. 3.9. The tested samples are drilled sideways for installation of thermocouples. After the processed surfaces are cleaned and their topographic parameters are measured properly, the surfaces are stacked together between a heat source and a heat sink. The role of the ball bearings is to minimize the effect due to misalignment. The radiation shield is employed to reduce the radial heat transfer from the test specimens by radiation. Thus, in a vacuum environment heat is only allowed to flow axially through the specimens. As a uniform heat flux is introduced by the heat source, the temperatures at the interface between the two samples in contact are determined by extrapolating the temperature measurements in the specimens. The temperature drop, ΔT , is then determined with the facility and the thermal contact conductance can be obtained by Eq. 2.1. Miller and Fletcher [28] explain each major component of this measuring facility in more detail.

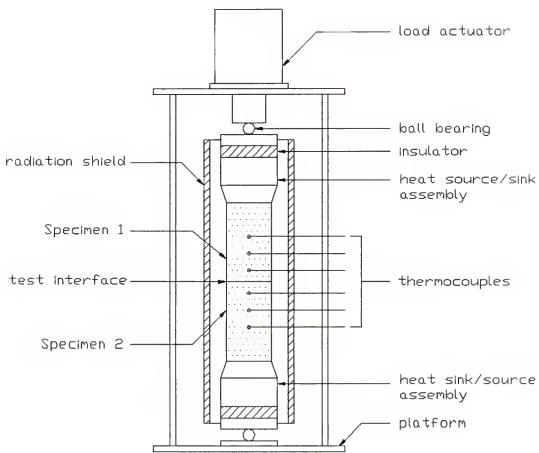


Fig. 3.9 Schematic of experimental test facility

3.3.2 Sources of Experimental Data

A large number of references of experimental measurements of thermal contact conductance can be found in the literature where correlations are given. Tien [29] listed twelve different experimental studies on which correlation was performed. They included tests of aluminum and stainless steel specimens in a vacuum environment. References to tests under the presence of various kinds of interstitial fluids, such as air, oil, argon, helium, and paraffin, were provided in Veziroglu's correlation study [30].

A comprehensive test of the thermal contact conductance was recently conducted by Hegazy [31]. The surface properties were characterized in detail and the specimens tested include Nickel 200, Stainless Steel 304, Zircaloy-4, and Zirconium-2.5%-Nb. The experiments were carried out in vacuum, nitrogen, and helium environments.

Surface roughness is commonly identified by the measurements of standard deviation of the surface height, σ , and the mean surface slope, m . However, the surface slope was not commonly reported in most early experimental works so that the use of their data is rather limited. A correlation performed by Antonetti and Whittle [32] is worth noting. They gathered published topographic data for 65 specimens to establish the relationship between the average roughness and the root-mean-square asperity slope. The resultant correlation can also be expressed in terms of the standard deviation of the surface roughness, σ , in micrometers and the mean asperity slope, m , by

$$m = 0.124 \sigma^{0.743} \quad (3.11)$$

For the modified Greenwood and Williamson model, in which spherical asperities are used, σ and m are not sufficient to characterize the surface topography. The three spectral moments m_{00} , m_{02} , and m_{04} are the fundamental parameters needed. At present, the only investigation in which both the spectral moments and the thermal contact conductance data are reported is the reference by McWaid and Marschall [24].

The numerical results by the Boltzmann statistics-based models are compared to the data reported in some of the references quoted above. Only those experiments conducted in vacuum will be compared as shown in Chapter 7.

CHAPTER 4

THEORETICAL BASIS FOR THE USE OF STATISTICAL MECHANICS

Statistical mechanics has never been attempted in the prediction of thermal contact conductance. In fact, the problem domain of the contact conductance can be readily explored by means of statistical mechanics. The purpose of this chapter is to demonstrate this applicability from the microscopic point of view.

In principle, if an observable property of a many particle system at a state of equilibrium can be characterized by a small number of other macroscopic properties, this observable property can often be described by statistical mechanics. This analysis also provides a microscopic description of the system (distribution of particles). Frequently, statistical mechanics is illustrated by applying it to equilibrium thermodynamic quantities. An illustrative example in statistical thermodynamics is further introduced in this chapter in order to establish the explicit links between thermal contact conductance and statistical mechanics.

4.1 Microscopic and Macroscopic Points of View in Contact Conductance

The mechanical and thermal mechanisms for metallic surfaces in contact in vacuum have been discussed in Chapter 2. The macroscopic or observable properties involved in this system are mainly the loading interfacial pressure and the thermal contact

conductance. As one studies the system microscopically, it is rather obvious that the applied load at the interface is distributed over the contact spots formed by the surface asperities (analogous to particles). These asperities on opposing surfaces are first brought into contact and they are deformed until they reach a state of force "equilibrium."

A thermal contact resistance, an observable property, arises as the heat is limited to flow through these contact spots. Substantial experimental studies have shown that, for surfaces of given material properties and topographic characteristics, the reduction of contact resistance behaves orderly and consistently as the loading pressure increases. Therefore, it is believed that the distribution of the contact spots is highly repeatable when the surfaces are brought into contact under a specific loading pressure condition. In other words, the contact conductance can be considered a result of "the most probable distribution" of contacts. From this perspective, statistical mechanics is indeed an appropriate method to predict the thermal contact conductance.

4.2 Boltzmann Statistics and Thermodynamics

Boltzmann statistical model is used repeatedly in this study to obtain first the most probable distribution of the surface summit heights, which is, in turn, used in the analysis of the distribution of contact spots at various loading pressures. This statistical model is briefly introduced here from a statistical thermodynamics viewpoint. The detailed discussion can be found in the reference by Sonntag and Van Wylen [33].

Consider a system comprised of N particles which are independently distributed among various energy levels. At the energy level u_j , there is a corresponding statistical weight g_j , which is the number of quantum states having that energy. For Boltzmann statistics, it is assumed that all these particles are distinguishable and there is no limit on the number of particles per quantum state. Then, the number of ways that a given distribution can arise is given by the formula

$$w = N! \prod_j \left(\frac{g_j^{N_j}}{N_j!} \right)$$

where N_j is the number of particles having energy u_j .

The quantity w given above is commonly known as the thermodynamic probability.

The product \prod can be removed by taking logarithm of both sides of the equation, giving

$$\ln w = N \ln N + \sum_j (N_j \ln g_j - N_j \ln N_j) \quad (4.1)$$

The two constraints which govern the activity of the particles in a closed system under an equilibrium state in thermodynamics are 1) the total number of particles must be conserved, i.e.,

$$\sum_j N_j = N \quad (4.2)$$

and 2) the internal energy must be conserved, i.e.,

$$\sum_j N_j u_j = U \quad (4.3)$$

To find the most probable distribution of particles N_j , which is the distribution that gives the highest thermodynamic probability, the following mathematical procedures are performed.

First, differentiate Eq. 4.1 and set it to zero. It follows that

$$d(\ln w) = \sum_j (g_j dN_j - \ln g_j dN_j - dN_j) = 0 \quad (4.4)$$

Furthermore, since N and U in Eqs. 4.2 and 3 are constants, the derivatives of these equations give

$$\sum_j dN_j = dN = 0 \quad (4.5)$$

and

$$\sum_j u_j dN_j = dU = 0 \quad (4.6)$$

Equation 4.4 can thus be simplified by using Eq. 4.5 as

$$d(\ln w) = \sum_j \ln \left(\frac{g_j}{N_j} \right) dN_j = 0 \quad (4.7)$$

At this point, the expression giving the maximum of w can be found by the method of Lagrange multipliers. Equations 4.5 and 6 are multiplied respectively by arbitrary values α and β and added together. Then, subtracting Eq. 4.7 from the sum gives

$$\sum_j \left(\ln \frac{N_j}{g_j} + \alpha + \beta u_j \right) dN_j = 0 \quad (4.8)$$

The only way that Eq. 4.8 can be satisfied is for each of the coefficients to be identically zero, or

$$\ln \frac{N_j}{g_j} + \alpha + \beta u_j = 0$$

Alternatively, it can be written in the form commonly known as the Boltzmann distribution law

$$N_j = g_j e^{-\alpha} e^{-\beta u_j} \quad (4.9)$$

Finally, the above equation can be further simplified by eliminating α by Eq. 4.2 (Constraint 1). Hence, the most probable distribution is obtained as

$$N_j = \frac{N g_j e^{-\beta u_j}}{\sum_j g_j e^{-\beta u_j}} \quad (4.10)$$

When the discrete variables u_j and g_j are so closely-spaced as to form a continuum, the summation is changed to an integration. This is a transformation means of the Euler-Maclaurin summation formula. Consequently, Eq. 4.10 is changed to the following

$$\frac{dN_u}{Ndu} = \frac{g_u e^{-\beta u}}{\int_0^\infty g_u e^{-\beta u} du} \quad (4.11)$$

In practice, the computation of the integral can be accomplished either analytically or numerically.

4.3 Comparison between Contact Conductance and Statistical Thermodynamics

Attention is now turned to the comparison of the features associated with the contact conductance and the counterpart in statistical thermodynamics given above to demonstrate their similarities. They are identified and listed side-by-side in Table 4.1. This table should provide the rationale of determining the contact conductance by statistical mechanics.

Undoubtedly, due to the similarities provided, the mathematics given in this chapter is to be performed as the Boltzmann statistical model is applied to the prediction of the contact conductance. Yet, an appropriate statistical weight function has not been defined. Chapter 6 will give the details of the derivation of four statistical weights and their formulated distributions of contacts.

Table 4.1 Similarities between the domain of statistical thermodynamics and that of thermal contact conductance

	Statistical Thermodynamics	Thermal Contact Conductance
1	Gas particles are independent of each other	Asperities are independent of each other
2	Number of particles is conserved in a closed system, $\sum_j N_j = N$	Number of asperities present on each surface is conserved, $\sum_j N_j = N$
3	Total energy is conserved, $\sum_j N_j u_j = U$	Sum of loads carried by asperities equals the applied force, $\sum_j N_j F_j = P$
4	Most probable distribution of particles is found by the Boltzmann statistical model; other system characteristics can be determined accordingly	Most probable distribution of true contact areas is found by the Boltzmann statistical model; thermal contact conductance can be determined accordingly

CHAPTER 5
MOST PROBABLE DISTRIBUTION OF SUMMIT HEIGHTS
BY BOLTZMANN STATISTICAL MODEL

Before studying the interaction between two contacting surfaces, one should identify the statistical features of each surface. Indeed, statistical mechanics can play a vital role in determining the distribution of the summit heights, which is commonly assumed Gaussian.

5.1 Surface Measurement as Constraints

The topography of a surface is often characterized by the use of a profilometer. As the stylus of a profilometer travels along a straight line on a surface, the electro-mechanical transducer produces electrical signals proportional to the variation of the surface heights. The actual surface profile can also be drawn by a chart recorder. For some surface preparation techniques, such as sandblasting, the profilometer tends to measure a consistent value of standard deviation.

Still, the above measurements cannot furnish the detailed statistics of the summit heights because the stylus trace can pass over an asperity shoulder rather than its summit. The variation of the summit heights is rarely measured due to the difficulty in setting up the instruments. Nevertheless, Williamson [34,35] implemented an unconventional

scheme to examine several surface texture parameters, including the summit heights. This technique is simple to understand but hard to perform. In principle, this method creates a contour map of a surface by displaying many closely-spaced parallel profiles in a two-dimensional array. Then, the summit of each asperity can be located. The major difficulty in this method is in maintaining a unique reference height of all profiles. This problem is solved by an auxiliary stylus-lifter built by Williamson.

One of the examples studied by Williamson is a bead-blasted aluminum surface, whose texture is highly homogeneous and isotropic. Both the surface heights and the summit heights on this surface are reported. The data show that there is a constant shift S on their distribution curves as shown in Fig. 5.1. This result gives the indication that the summit heights and surface heights should have the same standard deviation,

$$\sigma_{\text{asperity}} = \sigma_{\text{surface}} = \sigma_{\text{measured}}$$

and their mean values, μ , differ by the value of S ,

$$\mu_{\text{asperity}} - \mu_{\text{surface}} = S$$

The discussion given above suggests that a bead-blasted surface possesses the following characteristics:

1) Density of asperities,

$$\sum_j N_j = N \quad (5.1)$$

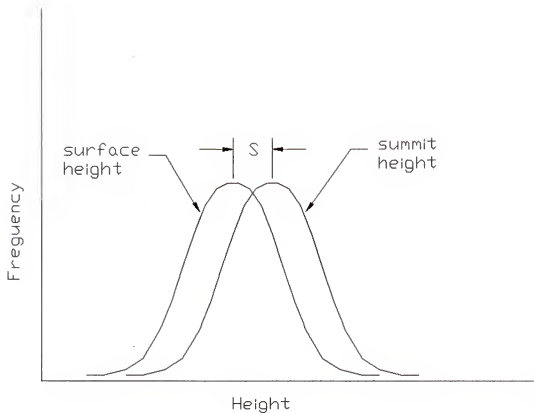


Fig. 5.1 Distributions of surface heights and summit heights of a bead-blasted surface

2) Mean summit height,

$$\sum_j N_j x_j = N \mu \quad (5.2)$$

3) Standard deviation of summit heights,

$$\sum_j N_j (x_j - \mu)^2 = N \sigma^2 \quad (5.3)$$

where N = density of asperities (number per unit area)
 N_j = density of asperities having summit height x_j
 x_j = particular summit height

These relationships can serve as the constraints imposed on the surface topography.

5.2 Derivation by Boltzmann Statistical Model

The Boltzmann statistical model is used to find the most probable distribution of summit heights. The mathematical procedures given in Section 4.2 are used. The derivatives of the constraints are:

$$1) \quad \sum_j dN_j = 0 \quad (5.4)$$

$$2) \quad \sum_j x_j dN_j = 0 \quad (5.5)$$

$$3) \quad \sum_j (x_j - \mu)^2 dN_j = 0 \quad (5.6)$$

Equation 5.6 can be expanded into

$$\sum_j x_j^2 dN_j - 2\mu \sum_j x_j dN_j + \mu^2 \sum_j dN_j = 0$$

The second and the third terms have been shown to be zero by Eqs. 5.5 and 4, respectively. Thus, the derivative of the third constraint becomes

$$\sum_j x_j^2 dN_j = 0 \quad (5.7)$$

Applying multipliers α , β , and γ to Eqs. 5.4, 5, and 7, respectively, and following the mathematics given in Eqs. 4.7, 8, and 9, one can obtain the Boltzmann distribution as

$$N_j = g_j e^{-\alpha} e^{-\beta x_j} e^{-\gamma x_j^2} \quad (5.8)$$

Substituting Eq. 5.8 into Eq. 5.1 yields

$$e^{-\alpha} = \frac{N}{\sum_j g_j e^{-\beta x_j} e^{-\gamma x_j^2}}$$

Thus, the multiplier α can be eliminated in Eq. 5.8 and the distribution becomes

$$N_j = \frac{N g_j e^{-\beta x_j} e^{-\gamma x_j^2}}{\sum_j g_j e^{-\beta x_j} e^{-\gamma x_j^2}} \quad (5.9)$$

Substituting this N_j into constraints 2 and 3 (Eqs. 5.2 and 3) yields

$$\frac{\sum_j g_j e^{-\beta x_j} e^{-\gamma x_j^2} x_j}{\sum_j g_j e^{-\beta x_j} e^{-\gamma x_j^2}} = \mu \quad (5.10)$$

and

$$\frac{\sum_j g_j e^{-\beta x_j} e^{-\gamma x_j^2} (x_j - \mu)^2}{\sum_j g_j e^{-\beta x_j} e^{-\gamma x_j^2}} = \sigma^2 \quad (5.11)$$

Further, applying Euler-Maclaurin summation formula to convert the above discrete forms to continuous forms yields

$$\frac{dN_x}{Ndx} = \frac{g_x e^{-\beta x} e^{-\gamma x^2}}{\int_0^\infty g_x e^{-\beta x} e^{-\gamma x^2} dx} \quad (5.12)$$

$$\frac{\int_0^\infty g_x e^{-\beta x} e^{-\gamma x^2} x dx}{\int_0^\infty g_x e^{-\beta x} e^{-\gamma x^2} dx} = \mu \quad (5.13)$$

and

$$\frac{\int_0^\infty g_x e^{-\beta x} e^{-\gamma x^2} (x - \mu)^2 dx}{\int_0^\infty g_x e^{-\beta x} e^{-\gamma x^2} dx} = \sigma^2 \quad (5.14)$$

As the summit height x is statistically weighted evenly, g_x is a constant. Then, Eqs. 5.12, 13, and 14 become

$$\frac{dN_x}{N dx} = \frac{e^{-\beta x} e^{-\gamma x^2}}{\int_0^{\infty} e^{-\beta x} e^{-\gamma x^2} dx} \quad (5.15)$$

$$\frac{\int_0^{\infty} e^{-\beta x} e^{-\gamma x^2} x dx}{\int_0^{\infty} e^{-\beta x} e^{-\gamma x^2} dx} = \mu \quad (5.16)$$

and

$$\frac{\int_0^{\infty} e^{-\beta x} e^{-\gamma x^2} (x - \mu)^2 dx}{\int_0^{\infty} e^{-\beta x} e^{-\gamma x^2} dx} = \sigma^2 \quad (5.17)$$

Here, the two unknown multipliers, β and γ , are obtained by solving Eqs. 5.16 and 17.

First, the integral in the denominator is performed exactly as

$$= \frac{\sqrt{\pi}}{2\sqrt{\gamma}} e^{\frac{\beta^2}{4\gamma}} \left[\lim_{x \rightarrow \infty} \operatorname{erf} \left(\sqrt{\gamma}x + \frac{\beta}{2\sqrt{\gamma}} \right) - \operatorname{erf} \left(\frac{\beta}{2\sqrt{\gamma}} \right) \right] \quad (5.18)$$

At this point, two hypotheses are made to simplify the derivation and their validations are provided later. Hypothesis 1 is given as

$$\operatorname{erf}\left(\frac{\beta}{2\sqrt{\gamma}}\right) \approx -1 \quad (5.19)$$

Thus, Eq. 5.18 becomes

$$\int_0^{\infty} e^{-\beta x} e^{-\gamma x^2} dx = \sqrt{\frac{\pi}{\gamma}} e^{\frac{\beta^2}{4\gamma}} \quad (5.20)$$

Using integration by parts and Eq. 5.20, one can solve the numerators in Eqs. 5.16 and 17 as

$$\int_0^{\infty} e^{-\beta x} e^{-\gamma x^2} x dx = -\frac{1}{2\gamma} \left(-1 + \beta \sqrt{\frac{\pi}{\gamma}} e^{\frac{\beta^2}{4\gamma}} \right) \quad (5.21)$$

and

$$\begin{aligned} & \int_0^{\infty} e^{-\beta x} e^{-\gamma x^2} (x-\mu)^2 dx \\ &= \left(-\frac{\beta}{2\gamma} - 2\mu \right) \left(\frac{1}{2\gamma} \right) + \left[\left(-\frac{\beta}{2\gamma} - 2\mu \right) \left(-\frac{\beta}{2\gamma} \right) + \left(\frac{1}{2\gamma} + \mu^2 \right) \right] \left(\sqrt{\frac{\pi}{\gamma}} e^{\frac{\beta^2}{4\gamma}} \right) \end{aligned} \quad (5.22)$$

Substituting Eqs. 5.20, 21, 22 into Eqs. 5.16 and 17 yields

$$\frac{1}{2\gamma} \cdot \frac{1}{\sqrt{\frac{\pi}{\gamma}} e^{\frac{\beta^2}{4\gamma}}} + \left(-\frac{\beta}{2\gamma} - \mu \right) = 0 \quad (5.23)$$

and

$$-\frac{\frac{\beta}{2\gamma} + 2\mu}{2\gamma} \cdot \frac{1}{\sqrt{\frac{\pi}{\gamma} e^{\frac{\beta^2}{4\gamma}}}} + \left[\left(\frac{\beta}{2\gamma} + 2\mu \right) \left(\frac{\beta}{2\gamma} \right) + \left(\frac{1}{2\gamma} - \mu^2 \right) - \sigma^2 \right] = 0 \quad (5.24)$$

Hypothesis 2 is stated that the polynomial terms are dominant so that the exponential terms are neglected in Eqs. 5.23 and 24. Thus, the two equations become

$$\frac{\beta}{2\gamma} + \mu = 0 \quad (5.25)$$

and

$$\left(\frac{\beta}{2\gamma} + 2\mu \right) \left(\frac{\beta}{2\gamma} \right) + \left(\frac{1}{2\gamma} - \mu^2 \right) - \sigma^2 = 0 \quad (5.26)$$

The above two equations are solved for the values of β and γ as

$$\beta = -\frac{\mu}{\sigma^2} \quad (5.27)$$

and

$$\gamma = \frac{1}{2\sigma^2} \quad (5.28)$$

The two hypotheses made are now to be validated. The values of β and γ are substituted into the left hand side of Eq. 5.19. This results in

$$erf\left(\frac{\beta}{2\sqrt{\gamma}}\right) = erf\left(-\frac{\mu}{\sqrt{2}\sigma}\right)$$

Surface measurement has shown μ is approximately 4σ [20], thus

$$\begin{aligned} \operatorname{erf}\left(\frac{\beta}{2\sqrt{\gamma}}\right) &= \operatorname{erf}(-2.9294) \\ &\approx -0.99993 \\ &\approx -1 \end{aligned}$$

Hence, Hypothesis 1 is validated.

The validation of Hypothesis 2 is accomplished by applying order-of-magnitude analyses on Eqs. 5.23 and 24. The results are as follows:

1) In Eq. 5.23, the analysis shows

$$\begin{aligned} \frac{1}{2\gamma} \frac{1}{\sqrt{\frac{\pi}{\gamma} e^{\frac{\beta^2}{4\gamma}}}} + \left(\frac{\beta}{2\gamma} - \mu \right) &= 0 \\ \frac{\sigma}{\sqrt{2\pi} e^{\frac{\mu^2}{2\sigma^2}}} + (\mu - \mu) &= 0 \\ \text{order of } \left(\frac{\sigma}{e^{\frac{\mu^2}{2\sigma^2}}} \right) &<< \text{order of } \mu \end{aligned}$$

2) In Eq. 5.24, the analysis shows

$$\begin{aligned} \frac{\frac{\beta}{2\gamma} + 2\mu}{2\gamma} \frac{1}{\sqrt{\frac{\pi}{\gamma} e^{\frac{\beta^2}{4\gamma}}}} + \left[\left(\frac{\beta}{2\gamma} + 2\mu \right) \left(\frac{\beta}{2\gamma} \right) + \left(\frac{1}{2\gamma} - \mu^2 \right) - \sigma^2 \right] &= 0 \\ \frac{(-\mu + 2\mu)\sigma^2}{\sqrt{2}} \frac{1}{\sqrt{\pi} e^{\frac{\mu^2}{2\sigma^2}}} + [(-\mu + 2\mu)(-\mu) + (\sigma^2 + \mu^2) - \sigma^2] &= 0 \\ \text{order of } \left(\frac{\mu\sigma^2}{e^{\frac{\mu^2}{2\sigma^2}}} \right) &<< \text{order of } \mu^2 \end{aligned}$$

Hence, Hypothesis 2 is validated.

Finally, by substituting the values of β , γ , and Eq. 5.20 into Eq. 5.15, the most probable distribution of summit heights is expressed by

$$\frac{dN_x}{Ndx} = f(x) = \frac{1}{\sqrt{2\pi}\sigma} e^{-\frac{1}{2}\left(\frac{x-\mu}{\sigma}\right)^2} \quad (5.29)$$

It is found that the above probability density function for the Boltzmann distribution is identical to the one for a Gaussian distribution. Hence, statistical mechanics has provided an analytical foundation to support the previously made assumption of Gaussian distribution of summit heights by Hsieh [20] and McWaid and Marschall [24].

CHAPTER 6

PREDICTION OF THERMAL CONTACT CONDUCTANCE BY BOLTZMANN STATISTICAL MODEL

In the preceding chapters, the important components of the thermal contact conductance and the Boltzmann statistical model have been reviewed. Using these as background, four predicting models will be developed.

As reviewed previously, alternative surface models (conical and spherical asperities) and deformation mechanisms (elastic and plastic) have been assumed by different investigators for the prediction of thermal contact conductance with reasonably accurate results. Thus, for a thorough exploration, the Boltzmann statistical model is applied in conjunction with the combinations of the above assumptions. Four different Boltzmann statistics-based models are then developed. This investigation attempts to identify the best surface model and asperity deformation mechanism in the statistical mechanics approach.

For simplicity, all models are set up on the basis of contacts of similar material and surface roughness. It is expected that the analytical models can be extended for the prediction of the conductance of contacts between dissimilar materials.

6.1 Development of Core Equations

Knowing the statistical distribution of summit heights on a surface, derived in Chapter 5, one can predict both the microscopic and macroscopic properties of surfaces in contact by the Boltzmann model. The formation of true contact areas are modeled as demonstrated in Fig. 6.1, where cones are selected for the shape of the asperities for illustration purpose. Figure 6.1a shows that the contact spots often occur near the summits as Williamson [34] found in his study. The first step in modeling is to represent each rough surface by the ideally shaped asperities as illustrated in Fig. 6.1b. As expected, perfect alignment between a pair of touching asperities rarely occurs. Nevertheless, it is believed that the degree of misalignments is statistically constant since the macroscopic properties, such as contact conductance, surface friction, etc., are consistently reproducible. It is thus justified to simplify the analysis by assuming that all touching asperities are perfectly aligned as illustrated in Fig. 6.1c. The theoretical prediction of the contact conductance can be corrected, if necessary, by a multiplying factor, which is close to unity [20].

Having the contact modeled as described, one is ready to apply the Boltzmann model to determine the distribution of contact spots. Intuitively, the size of a contact can be quantified by its radius. Alternatively, it can be represented implicitly by the summit penetration depth δ (see Fig. 6.1). The latter is preferred because the Boltzmann statistical model is constrained by the formula

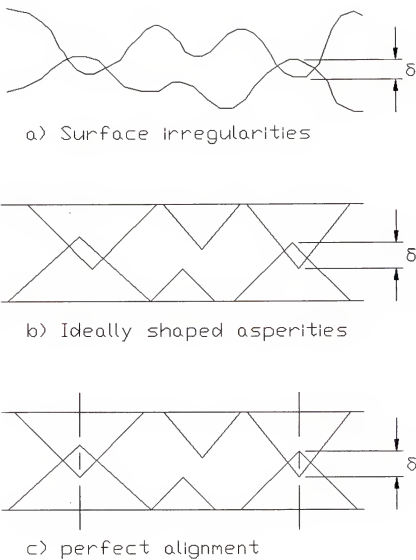


Fig. 6.1 Demonstration of modeling technique used in contact area formation

$$\sum_j N_j = N \quad (6.1)$$

where N = density of all summit penetrations (equal to density of asperities)
 N_j = density of summit penetrations of δ_j

If the corresponding asperities are not in contact, the value of δ is taken to be negative.

The other constraint imposed on the surfaces in contact is the force balance that must occur at the interface. According to the selected sign for δ , an asperity becomes a load carrier only when its relative penetration, δ , is positive. In general, the value of the contact spot radius a and the load F can be related to δ by the power laws

$$a_j = C_1 \delta_j^{C_2} \quad , \delta_j \geq 0 \quad (6.2)$$

and

$$F_j = \begin{cases} 0 & , \delta_j < 0 \\ C_3 \delta_j^{C_4} & , \delta_j \geq 0 \end{cases} \quad (6.3)$$

The coefficients C_i are dictated by the assumed asperity shape and the deformation mechanism. Since the force acting at the interface is to be carried by the discrete contact spots, one can write the force relation as

$$\sum_j N_j F_j = P$$

It follows that

$$\sum_j N_j C_3 \delta_j^{C_4} |_{\delta_j \geq 0} = P \quad (6.4)$$

To perform the mathematical procedures analogous to those in Section 4.2, the two constraints, Eqs. 6.1 and 4, are differentiated as

$$\sum_j dN_j = 0 \quad (6.5)$$

and

$$\sum_j dN_j \delta_j^{c_4} \Big|_{\delta_j \geq 0} = 0 \quad (6.6)$$

Suppose that there exists a statistical weight g_j which represents the number of ways having summit penetration δ_j . Application of Lagrange multipliers α and β to Eqs. 6.5 and 6, respectively, leads to a distribution law as follows

$$N_j = \begin{cases} g_j e^{-\alpha} & , \delta_j < 0 \\ g_j e^{-\alpha} e^{-\beta \delta_j^{c_4}} & , \delta_j \geq 0 \end{cases} \quad (6.7)$$

The variation of g_j is contributed by some interfacial contact features, such as the surface roughness and the assumed asperity shape and deformation manner. For that matter, different models are developed to model an interface as discussed in Section 3.2. Different statistical weights are proposed as formulated in the next four sections.

One returns to the Boltzmann analysis. The two multipliers can be related to each other by substituting Eq. 6.7 into Constraint 1 (Eq. 6.1) that yields

$$\sum_j N_j = \sum_j g_j e^{-\alpha} \Big|_{\delta_j < 0} + \sum_j g_j e^{-\alpha} e^{-\beta \delta_j^{c_4}} \Big|_{\delta_j \geq 0} = N$$

so that e^{-a} can be factored out, yielding

$$e^{-a} = \frac{N}{\sum_j g_j|_{\delta_j < 0} + \sum_j g_j e^{-\beta \delta_j^{C_4}}|_{\delta_j \geq 0}} \quad (6.8)$$

Then, substituting e^{-a} into Eqs. 6.7 and 4 gives respectively

$$N_j = \begin{cases} \frac{g_j N}{\sum_j g_j|_{\delta_j < 0} + \sum_j g_j e^{-\beta \delta_j^{C_4}}|_{\delta_j \geq 0}} & , \delta_j < 0 \\ \frac{g_j N e^{-\beta \delta_j^{C_4}}}{\sum_j g_j|_{\delta_j < 0} + \sum_j g_j e^{-\beta \delta_j^{C_4}}|_{\delta_j \geq 0}} & , \delta_j \geq 0 \end{cases} \quad (6.9)$$

and

$$\frac{\sum_j g_j N e^{-\beta \delta_j^{C_4}} C_3 \delta_j^{C_4}|_{\delta_j \geq 0}}{\sum_j g_j|_{\delta_j < 0} + \sum_j g_j e^{-\beta \delta_j^{C_4}}|_{\delta_j \geq 0}} = P \quad (6.10)$$

The Boltzmann statistical model in conjunction with the mechanical analysis has been used to derive the distribution of the summit penetration depths, which is virtually the distribution of the contact spots. The thermal analysis is then incorporated to obtain the total contact conductance. Including the effect of the constriction of heat flow channels, given by Eqs. 3.1, 3.5, and 6.2, the conductance can be written as

$$h = \frac{2k}{\psi} \sum_j N_j C_1 \delta_j^{C_1}|_{\delta_j \geq 0} \quad (6.11)$$

It is assumed that all contact spots are evenly-spaced such that the ratio of the spot radius to the flow channel radius, a/b (see Fig. 3.4), is the same for each spot. Since the constriction alleviation factor Ψ is a function of a/b , Ψ can be factored out from the summation sign as shown in this equation. The evaluation of the ratio a/b will be discussed later when the details of each Boltzmann statistics-based model are described. If N_j in Eq. 6.11 is replaced by Eq. 6.9, the predicted conductance becomes

$$h = \frac{2k}{\Psi} \cdot \frac{\sum_j g_j N e^{-\beta \delta_j^{C_4}} C_1 \delta_j^{C_2} \Big|_{\delta_j > 0}}{\sum_j g_j \Big|_{\delta_j < 0} + \sum_j g_j e^{-\beta \delta_j^{C_4}} \Big|_{\delta_j \geq 0}} \quad (6.12)$$

When all the discrete variables are numerous and closely-spaced, Euler-Maclaurin summation formula can be applied to change the summations in Eqs. 6.9, 10, and 12 into integrals. Then,

$$\frac{dN_\delta}{Nd\delta} = \begin{cases} \frac{g_\delta}{\int_{\delta < 0} g_\delta d\delta + \int_{\delta \geq 0} g_\delta e^{-\beta \delta^{C_4}} d\delta} & , \delta < 0 \\ \frac{g_\delta e^{-\beta \delta^{C_4}}}{\int_{\delta < 0} g_\delta d\delta + \int_{\delta \geq 0} g_\delta e^{-\beta \delta^{C_4}} d\delta} & , \delta \geq 0 \end{cases} \quad (6.13)$$

$$\frac{N \int_{\delta \geq 0} g_\delta e^{-\beta \delta^{C_4}} C_3 \delta^{C_4} d\delta}{\int_{\delta < 0} g_\delta d\delta + \int_{\delta \geq 0} g_\delta e^{-\beta \delta^{C_4}} d\delta} = P \quad (6.14)$$

and

$$h = \frac{2k}{\Psi} \cdot \frac{N \int_{\delta > 0} g_{\delta} e^{-\beta \delta^{C_i}} C_i \delta^{C_i} d\delta}{\int_{\delta < 0} g_{\delta} d\delta + \int_{\delta > 0} g_{\delta} e^{-\beta \delta^{C_i}} d\delta} \quad (6.15)$$

The three equations derived above are one-to-one functions with respect to the Lagrange multiplier β . It can thus serve as an intermediate variable which forms a link among the values of $dN_{\delta}/Nd\delta$, P , and h . In summary, the core equations for a Boltzmann statistics-based model are formulated and they can be solved by numerical integration.

As discussed earlier, the statistical weight function g_{δ} and the coefficients C_i depend on the surface model and the deformation mechanism. Since there are several possible ways to model the surface roughness and the asperity deformation (given in Section 3.2), g_{δ} and C_i are not unique. Four different models are analyzed in the sections that follows.

6.2 Plastic Cone Model

One of the ways to represent surface irregularities is by conical asperities and the summits of the touching asperities are deformed plastically. Major components of this modeling technique are introduced below.

a) Surface model

A rough surface is modeled by a flat plane covered with cones of same base angle and different heights as performed by Hsich [20]; see Fig. 3.5. Additionally, assuming

a Gaussian distribution of summit heights Hsieh can derive a list of surface characteristics relevant to this model. Some of the characteristics are summarized as follows:

1) Density of surface asperities (number per unit area),

$$N = \left(\frac{m}{7.308 \sigma} \right)^2 \quad (6.16)$$

2) Maximum summit height (peak-to-valley roughness),

$$x_{\max} = 8 \sigma \quad (6.17)$$

3) Mean summit height,

$$\mu = 4 \sigma \quad (6.18)$$

It is noted that the asperities having heights beyond x_{\max} above are within 0.02% of the total population of the asperities described by the derived Boltzmann distribution given in Eq. 5.29.

b) Deformation mechanism

In this model, the asperities are deformed following the Yovanovich model as illustrated in Fig. 6.2. When two asperities are brought into contact, their summits (overlapping regions) penetrate into each other and displace plastically. Similar to the case

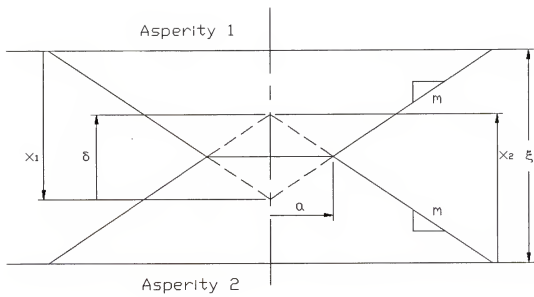


Fig. 6.2 Plastic deformation at asperity summits

where an indenter is forced into a material in a hardness test, the load is related to the real contact area by

$$F = HA_r = H\pi a^2 \quad (6.19)$$

From the geometry given in Fig. 6.2, the contact spot radius, a , can be written in terms of the summit penetration, δ , as

$$a = \frac{\delta}{2m} \quad (6.20)$$

so that Eq. 6.19 becomes

$$F = H\pi \left(\frac{\delta}{2m} \right)^2 = \frac{\pi H}{4m^2} \delta^2 \quad (6.21)$$

Comparing Eqs. 6.20 and 21 to Eqs. 6.2 and 3, respectively, one can determine the coefficients as

$$\begin{aligned} C_1 &= \frac{1}{2m} \\ C_2 &= 1 \\ C_3 &= \frac{\pi H}{4m^2} \\ C_4 &= 2 \end{aligned} \quad (6.22)$$

c) Statistical weight

The product of the statistical weight function g_δ and $d\delta$ is directly proportional to the probability of having a summit penetration depth between δ and $\delta + d\delta$. Thus, $g_\delta d\delta$ can be written as

$$g_\delta d\delta = C \times P(\delta \text{ to } \delta + d\delta) \quad (6.23)$$

This probability involves a combination of three events. They are the height of an asperity x_1 , the height of the opposing asperity x_2 , and the base plane separation ξ ; they are related to each other by

$$\delta = x_1 + x_2 - \xi \quad (6.24)$$

Thus,

$$P(\delta \text{ to } \delta + d\delta) = P(x_1 \cap x_2 \cap x_1, x_2 | \xi \text{ to } \xi + d\xi)$$

Since the load carrying asperities often meet at their summits as shown in Figs. 6.1 and 2, it is assumed that the height of an asperity is always larger than its deformed region so that the probability can be more specifically expressed by

$$P(\delta \text{ to } \delta + d\delta) = P(x_1 \geq \frac{\delta}{2} \cap x_2 \geq \frac{\delta}{2} \cap x_1, x_2 | \xi \text{ to } \xi + d\xi)$$

For any given x_1 and x_2 , the geometry in Fig. 6.2 shows that $d\delta/d\xi$ is a constant equal to -1, which is independent of δ . The three events are thus mutually exclusive as

$$P(\delta \text{ to } \delta + d\delta) = P(x_1 \geq \frac{\delta}{2} \cap x_2 \geq \frac{\delta}{2} \cap \xi \text{ to } \xi + d\xi)$$

which is

$$P(\delta \text{ to } \delta + d\delta) = P(x_1 \geq \frac{\delta}{2}) \times P(x_2 \geq \frac{\delta}{2}) \times P(\xi \text{ to } \xi + d\xi) \quad (6.25)$$

The first term $P(x_1 \geq \delta/2)$ can be defined as the portion of the apparent contact area covered by asperities of height greater than $\delta/2$. By using the probability density function given in Eq. 5.29, the following can be written

$$P(x_1 \geq \frac{\delta}{2}) = \frac{\pi N}{m^2} \int_{\delta/2}^{8\sigma} f(x_1) x_1^2 dx \quad (6.26)$$

The upper bound of the integral is the maximum summit height, 8σ , which is given by Eq. 6.17. When the two contacting surfaces have identical roughness, $P(x_1 \geq \delta/2)$ equals $P(x_1 \geq \delta/2)$.

Owing to the maximum summit height, 8σ , a contact is formed only if the base plane separation ξ is smaller than 16σ , which serves as the operating domain for this model. Thus, the last term is

$$P(\xi \text{ to } \xi + d\xi) = \frac{d\xi}{16\sigma}$$

Moreover, as mentioned earlier that $d\delta/d\xi$ is -1, the above equation becomes

$$P(\xi \text{ to } \xi + d\xi) = -\frac{d\delta}{16\sigma} \quad (6.27)$$

Combining Eqs. 6.23, 25, 26, and 27 gives

$$g_\delta d\delta = -\frac{C\pi^2 N^2}{16\sigma m^4} \left(\int_{\delta/2}^{8\sigma} f(x) x^2 dx \right)^2 d\delta$$

As given in Eqs. 6.14 and 15, only the proportion of g_δ is of interest. Thus, the constant preceding the parenthesis can be dropped, which will not affect the results of the total conductance versus the total load. It is thus simplified as

$$g_\delta = \left(\int_{\delta/2}^{8\sigma} f(x) x^2 dx \right)^2 \quad (6.28)$$

This expression is only applicable for the case in which δ is greater than zero, meaning that a contact is made. When δ is less than zero, g_δ is still dependent upon the heights of the asperities involved and the base plane separation. Figure 6.3 illustrates this situation. Following the geometrical relationship among x_1 , x_2 , ξ , and δ and the above procedures deriving g_δ , one can show that 1) when $-8\sigma \leq \delta < 0$,

$$g_\delta = \int_0^{8\sigma} f(x_1) x_1^2 \int_0^{16\sigma + \delta - x_1} f(x_2) x_2^2 dx_2 dx_1 \quad (6.29)$$

and 2) when $-16\sigma \leq \delta < -8\sigma$,

$$g_\delta = \int_0^{16\sigma + \delta} f(x_1) x_1^2 \int_0^{16\sigma - x_1} f(x_2) x_2^2 dx_2 dx_1 \quad (6.30)$$

The statistical weight g_δ is thus derived for the entire domain, $-16\sigma \leq \delta \leq 16\sigma$.

d) Constriction alleviation factor

The Gibson's expression, listed in Table 3.1, is selected to determine the constriction alleviation factor, Ψ , in Eq. 6.15. The independent variable of this expression is the ratio

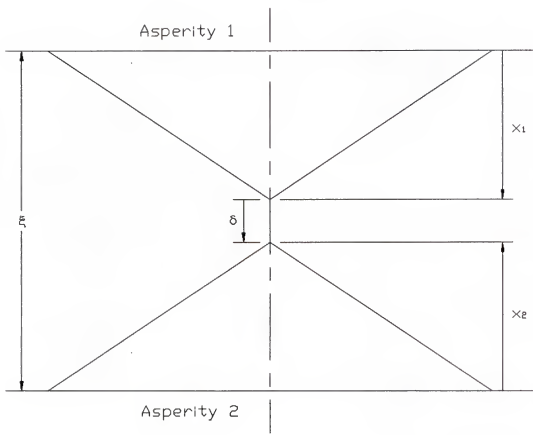


Fig. 6.3 Illustration of penetration depth for non-contacting asperities

of contact spot radius to flow channel radius, a/b , and it can be determined easily for this model. In this effort, one can denote each contact spot by an index integer i . The force balance requires that

$$\frac{\sum_i a_i^2}{\sum_i b_i^2} = \frac{P}{H}$$

It is assumed that the contact spots are evenly distributed so that the ratios a_i/b_i are identical for all spots. Then,

$$\frac{a}{b} = \sqrt{\frac{P}{H}} \quad (6.31)$$

In this equation, the loading pressure P has been given in Eq. 6.14.

e) Summary

At this point, all parameters involved are derived. For clarity sake, the final forms of the important equations are summarized. Substituting coefficients C_i in Eq. 6.22 into Eqs. 6.14 and 15 gives

$$P = \frac{\pi H}{4m^2} \cdot \frac{N \int_0^{16\sigma} g_\delta e^{-\beta\delta^2} \delta^2 d\delta}{\int_{-16\sigma}^{16\sigma} g_\delta d\delta + \int_0^{16\sigma} g_\delta e^{-\beta\delta^2} d\delta} \quad (6.32)$$

and

$$h = \frac{k}{m\Psi} \cdot \frac{N \int_0^{16\sigma} g_\delta e^{-\beta\delta^2} \delta d\delta}{\int_{-16\sigma}^{16\sigma} g_\delta d\delta + \int_0^{16\sigma} g_\delta e^{-\beta\delta^2} d\delta} \quad (6.33)$$

where

$$\Psi = \Psi \left(\sqrt{\frac{P}{H}} \right)$$

Combining Eqs. 6.28, 29, and 30 yields

$$g_{\delta} = \begin{cases} \left(\frac{8\sigma}{\int_{\delta/2}^{8\sigma} f(x)x^2 dx} \right)^2, & \delta \geq 0 \\ \int_0^{8\sigma} f(x_1)x_1^2 \int_0^{16\sigma-\delta-x_1} f(x_2)x_2^2 dx_2 dx_1, & -8\sigma \leq \delta < 0 \\ \int_0^{16\sigma-\delta} f(x_1)x_1^2 \int_0^{16\sigma-\delta-x_1} f(x_2)x_2^2 dx_2 dx_1, & -16\sigma \leq \delta < -8\sigma \end{cases} \quad (6.34)$$

where

$$f(x) = \frac{1}{\sqrt{2\pi}\sigma} e^{-\frac{1}{2}\left(\frac{x-\mu}{\sigma}\right)^2}$$

These equations conclude the development of the Boltzmann statistics-based plastic cone model.

6.3 Plastic Cone and Elastic Base Model

Similar to the plastic cone model above, the roughness of a surface can be modeled as cones with their summits deformed plastically. In addition, based on Hsieh, it is assumed that the base of a compressed asperity is deformed elastically by a deflection η as illustrated in Fig. 6.4 [20]. In this figure, the dashed lines represent the original shapes of the asperities prior to deformation.

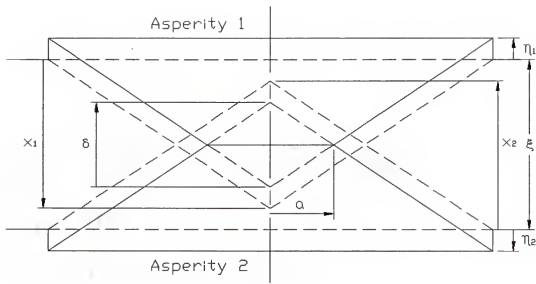


Fig. 6.4 Illustration of plastic summit and elastic base deformation

The majority of the equations formulated in the previous section remain valid, except $d\delta/d\xi$ which is no longer equal to -1. The geometry given in Fig 6.4 shows that

$$\delta = x_1 + x_2 - \xi - \eta_1 - \eta_2 \quad (6.35)$$

This difference affects the expression of g_s for $\delta \geq 0$. The relationship between $d\xi$ and $d\delta$ must be re-established.

The elastic base deflection, η , can be approximated by the result of a uniform distribution of pressure acting on the base plane over the asperity base area. The average deflection, η , is then derived and given by [26]

$$\eta = \frac{0.54(1-v^2)mF}{Ex} \quad (6.36)$$

Using Eq. 6.21,

$$\eta = \frac{0.54\pi(1-v^2)H\delta^2}{4Emx} \quad (6.37)$$

Thus, ξ can be written in terms of δ by substituting Eq. 6.37 into Eq. 6.35, yielding

$$\xi = -\delta + x_1 + x_2 - \frac{0.54\pi H(1-v^2)\delta^2}{4Em} \left(\frac{1}{x_1} + \frac{1}{x_2} \right) \quad (6.38)$$

Differentiating this equation with respect to δ gives

$$\frac{d\xi}{d\delta} = - \left\{ 1 + \frac{0.27\pi H(1-v^2)\delta}{Em} \left(\frac{1}{x_1} + \frac{1}{x_2} \right) \right\} \quad (6.39)$$

The negative sign can be omitted because only the proportion of g_δ is of interest. Thus,

$$\frac{d\xi}{d\delta} = 1 + \frac{0.27\pi H(1-v^2)\delta}{Em} \left(\frac{1}{x_1} + \frac{1}{x_2} \right) \quad (6.40)$$

Unlike the previous model, $d\delta/d\xi$ is not a constant for $\delta \geq 0$. The statistical weight function cannot be simplified and

$$g_\delta = \int_{\delta/2}^{8\sigma} f(x_1) x_1^2 \int_{\delta/2}^{8\sigma} f(x_2) x_2^2 \frac{d\xi}{d\delta} dx_2 dx_1 \quad (6.41)$$

For the entire range of δ , g_δ can be expressed by

$$g_\delta = \begin{cases} \int_{\delta/2}^{8\sigma} f(x_1) x_1^2 \int_{\delta/2}^{8\sigma} f(x_2) x_2^2 \frac{d\xi}{d\delta} dx_2 dx_1 & , \delta \geq 0 \\ \int_0^{8\sigma} f(x_1) x_1^2 \int_0^{16\sigma + \delta - x_1} f(x_2) x_2^2 dx_2 dx_1 & , -8\sigma \leq \delta < 0 \\ \int_0^{16\sigma + \delta} f(x_1) x_1^2 \int_0^{16\sigma + \delta - x_1} f(x_2) x_2^2 dx_2 dx_1 & , -16\sigma \leq \delta < -8\sigma \end{cases} \quad (6.42)$$

In summary, the conclusive equations for this model include Eqs. 6.32, 33, and 42 combined with Eq. 6.40 for $d\xi/d\delta$.

6.4 Elastic Spherical Asperity Model

Conical asperities have been employed to represent the irregularities of a rough surface. Indeed, several investigations demonstrate that modeling the roughness by spherical asperities also leads to reasonable analytical results. One example is the modified Greenwood and Williamson model, developed by McWaid and Marschall [24] and briefly discussed in Section 3.2.4. In the present Boltzmann statistics-based model, a great deal of attributes used by McWaid and Marschall are employed. Details are discussed below.

a) Surface model

The techniques of random process theory were first used in the studies of ocean surfaces. Nayak then extended this approach to analyze the statistics of a rough surface by using the power spectral density of a surface profile [36]. Comprehensive derivations of surface geometric parameters can be found in the publications by Nayak [36] and Bush et al. [37]. Some of these parameters suitable for a predicting model for contact conductance are the density of asperities (number per unit area),

$$D = \frac{mo_4}{6\sqrt{3}\pi mo_2} \quad (6.43)$$

the mean radius of summits,

$$R = \frac{3\sqrt{\pi}}{8\sqrt{mo_4}} \quad (6.44)$$

and the standard deviation of summit heights,

$$\sigma = \sqrt{\left(1 - \frac{0.8968}{\rho}\right) mo_0} \quad (4.45)$$

The fundamental variables mo_0 , mo_2 , mo_4 , and ρ , mentioned before in Section 3.2.4, are the zeroth, second, fourth moments of the power spectral density, and the bandwidth parameter, respectively. The physical meanings of mo_0 , mo_2 , and mo_4 are the variances of the surface height, the slope, and the curvature of a profilometric sketch, respectively.

As described, mo_0 is the square of the standard deviation of profile height, which is commonly obtained by a surface profilometer. Devices measuring the root mean square of surface slope, which is $mo_2^{1/2}$, although not as popular, are also commercially available. The major issue is to obtain mo_4 for a surface. The practical difficulties of this measurement involve the choices of sample spacing and signal processing [38].

Regardless of the stated technical difficulties, mo_2 and mo_4 can still be obtained by primitive techniques. Nayak shows that not only the density of asperities, D , but also the density of zero-crossings D_{zero} and the density of extrema D_{ext} (peaks and valleys) of a profile can be expressed in terms of mo_2 and mo_4 [36]. Inversely, mo_2 and mo_4 are written in terms of D_{zero} and D_{ext} as

$$mo_2 = \pi^2 mo_0 D_{zero}^2 \quad (4.46)$$

$$mo_4 = \pi^4 mo_0 D_{zero}^2 D_{ext}^2 \quad (4.47)$$

and

Then, by counting the number of zero-crossings, peaks, and valleys of a surface profile, one can determine $m_0{}_2$ and $m_0{}_4$.

b) Deformation mechanism

When two spherical asperities are pressed together and meet at their summits, Hertzian theory provides a thorough analysis of the asperities under elastic deformation [26]. Figure 6.5 depicts the deformation scheme of this kind. The original shape of each asperity is drawn by the dashed line and the elastically deformed asperities are drawn by the solid lines. For two contacting spheres having the same radius, Hertzian theory predicts that

$$\delta = \frac{2a^2}{R}$$

and

$$F = \frac{4Ea^3}{3R(1 - v^2)}$$

Recasting the δ equation as to

$$a = \sqrt{\frac{R}{2}} \delta^{0.5} \quad (6.48)$$

and using it in the F equation above gives

$$F = \frac{\sqrt{2R} E}{3(1 - v^2)} \delta^{1.5} \quad (6.49)$$

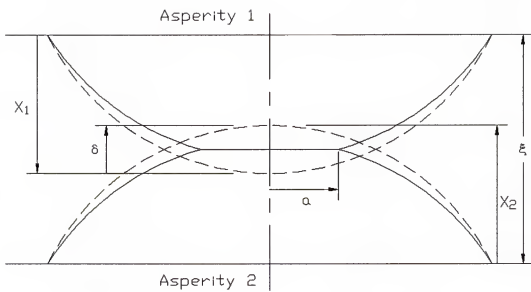


Fig. 6.5 Material deformation between spherical asperities

From these two equations, the coefficients in Eqs. 6.2 and 3 can be determined as

$$\begin{aligned}
 C_1 &= \sqrt{\frac{R}{2}} \\
 C_2 &= 0.5 \\
 C_3 &= \frac{\sqrt{2R}E}{3(1 - v^2)} \\
 C_4 &= 1.5
 \end{aligned} \tag{6.50}$$

c) Statistical weight

Similar to the plastic cone model, the summit heights, x_1 and x_2 , the base plane separation, ξ , and the summit separation, δ , are related by Eq. 6.24

$$\delta = x_1 + x_2 - \xi$$

Therefore, for given x_1 and x_2 , $d\delta/d\xi$ equals -1. Following the reasoning given in the plastic cone model, Section 6.2, the statistical weight function expressed by Eq. 6.34 can be again derived.

d) Constriction alleviation factor

Since it is assumed that for all contacts the spot radius to flow channel radius ratios are equal to each other, this leads to

$$\frac{a}{b} = \frac{\sum_i a_i}{\sum_i b_i} = \sqrt{\frac{\sum_i \pi a_i^2}{\sum_i \pi b_i^2}}$$

The right hand side of this equation physically means the square root of the ratio of true contact area to apparent contact area. Therefore, a/b can be alternatively written as

$$\frac{a}{b} = \sqrt{\sum_j N_j \pi (C_1 \delta_j^{C_2})^2}$$

Hence,

$$\frac{a}{b} = \left(\frac{\pi N \int_0^{16\sigma} g_\delta e^{-\beta \delta^{C_2}} (C_1 \delta^{C_2})^2 d\delta}{\int_{-16\sigma}^0 g_\delta d\delta + \int_0^{16\sigma} g_\delta e^{-\beta \delta^{C_2}} d\delta} \right)^{0.5} \quad (6.51)$$

e) Summary

Substituting the coefficients from Eq. 6.50 into Eqs. 6.14, 6.15, and 6.51 results in

$$P = \frac{\sqrt{2R}E}{3(1-v^2)} \cdot \frac{N \int_0^{16\sigma} g_\delta e^{-\beta \delta^{1.5}} \delta^{1.5} d\delta}{\int_{-16\sigma}^0 g_\delta d\delta + \int_0^{16\sigma} g_\delta e^{-\beta \delta^{1.5}} d\delta} \quad (6.52)$$

$$h = \frac{\sqrt{2R}k}{\Psi} \cdot \frac{N \int_0^{16\sigma} g_\delta e^{-\beta \delta^{1.5}} \delta^{0.5} d\delta}{\int_{-16\sigma}^0 g_\delta d\delta + \int_0^{16\sigma} g_\delta e^{-\beta \delta^{1.5}} d\delta} \quad (6.53)$$

and

$$\frac{a}{b} = \left(\frac{\pi R}{2} \cdot \frac{N \int_0^{16\sigma} g_\delta e^{-\beta \delta^{1.5}} d\delta}{\int_{-16\sigma}^{16\sigma} g_\delta d\delta + \int_0^{16\sigma} g_\delta e^{-\beta \delta^{1.5}} d\delta} \right)^{0.5} \quad (6.54)$$

where g_δ is obtained by Eq. 6.34 and $\Psi(a/b)$ is obtained by the Gibson's expression (see Table 3.1).

6.5 Elastic and Plastic Spherical Asperity Model

In addition to elastic deformation, continuous loading of a spherical asperity may cause a transformation from elastic to plastic deformation at the summit. From the work of Tabor based on his ball indentation hardness test, the plastic deformation begins when the maximum Hertzian pressure p_0 reaches 60% of the indentation hardness [27],

$$p_0 = 0.6H \quad (6.55)$$

The pressure, p_0 , occurs at the center of the contact spot and its value relates to the loading force, F , and the spot radius, a , by [26]

$$p_0 = \frac{3F}{2\pi a^2}$$

This equation can be expressed in terms of δ by substituting for a and F from Eqs. 6.48 and 49, respectively. Thus,

$$P_0 = \frac{\sqrt{2\delta}E}{\pi(1-v^2)\sqrt{R}} \quad (6.56)$$

Using Eq. 6.55, the onset of plastic deformation becomes

$$\frac{\sqrt{2\delta}E}{\pi(1-v^2)\sqrt{R}} = 0.6H$$

which can be recast as

$$\delta = 1.7765 \frac{H^2(1-v^2)^2R}{E^2}$$

The plastically deformed region, surrounded by elastic material, grows as the summit penetration, δ , increases from the amount given above. For convenience, a higher criterion of δ for detectable plastic flow is selected as a critical transition from a wholly elastic mode to a wholly plastic mode of material deformation. Thus,

$$\delta_c = \frac{2H^2(1-v^2)^2R}{E^2} \quad (6.57)$$

The summits of a pair of contacting asperities thus undergo elastic or plastic deformation depending on their penetration depth, δ . When δ is less than the δ_c , the load supported by the elastic material is given by Eq. 6.49. Once δ exceeds δ_c , plastic deformation becomes dominant so that

$$F = H\pi a^2 = \frac{\pi HR}{2} \delta \quad (6.58)$$

In summary, the loading force is

$$F = \begin{cases} 0 & , \delta < 0 \\ \frac{\sqrt{2RE}}{3(1 - v^2)} \delta^{1.5} & , 0 \leq \delta < \delta_c \\ \frac{\pi HR}{2} \delta & , \delta \geq \delta_c \end{cases} \quad (6.59)$$

Comparing Eq. 6.59 to Eq. 6.3, one can determine the values of the coefficients C_3 and C_4 and derive them in two groups of δ as follows:

1) For $0 \leq \delta < \delta_c$, C_3 and C_4 can be found in Eq. 6.50

$$C_3 = \frac{\sqrt{2RE}}{3(1 - v^2)}$$

$$C_4 = 1.5$$

2) For $\delta \geq \delta_c$,

$$C_3 = \frac{\pi HR}{2}$$

$$C_4 = 1 \quad (6.60)$$

Finally, the loading pressure, P , and the total thermal contact conductance, h , can be written by substituting all the above coefficients into Eqs. 6.14 and 15 as

$$P = \frac{\frac{\sqrt{2RE}}{3(1 - v^2)} N \int_0^{\delta_c} g_\delta e^{-\beta \delta^{1.5}} \delta^{1.5} d\delta + \frac{\pi HR}{2} N \int_{\delta_c}^{16\sigma} g_\delta e^{-\beta \delta} \delta d\delta}{\int_0^{\delta_c} g_\delta d\delta + \int_0^{\delta_c} g_\delta e^{-\beta \delta^{1.5}} d\delta + \int_{\delta_c}^{16\sigma} g_\delta e^{-\beta \delta} d\delta} \quad (6.61)$$

and

$$h = \frac{\sqrt{2R}k}{\Psi} \cdot \frac{N \int_0^{\delta_c} g_\delta e^{-\beta \delta^{1.5}} \delta^{0.5} d\delta + N \int_{\delta_c}^{16\sigma} g_\delta e^{-\beta \delta} \delta^{0.5} d\delta}{\int_{-16\sigma}^0 g_\delta d\delta + \int_0^{\delta_c} g_\delta e^{-\beta \delta^{1.5}} d\delta + \int_{\delta_c}^{16\sigma} g_\delta e^{-\beta \delta} d\delta} \quad (6.62)$$

The value of a/b , needed for the Gibson's constriction alleviation factor equation, is obtained from Eq. 6.51 as

$$\frac{a}{b} = \left(\frac{\pi R}{2} \cdot \frac{N \int_0^{\delta_c} g_\delta e^{-\beta \delta^{1.5}} \delta d\delta + N \int_{\delta_c}^{16\sigma} g_\delta e^{-\beta \delta} d\delta}{\int_{-16\sigma}^0 g_\delta d\delta + \int_0^{\delta_c} g_\delta e^{-\beta \delta^{1.5}} d\delta + \int_{\delta_c}^{16\sigma} g_\delta e^{-\beta \delta} d\delta} \right)^{0.5} \quad (6.63)$$

The statistical weight g_δ remains the same as in Eq. 6.34.

CHAPTER 7

NUMERICAL RESULTS AND DISCUSSION

The equations necessary to predict the thermal contact conductance have been formulated in the previous chapter. Finding the analytical solutions to these equations is not successful because of the difficulty of evaluating the multiple integrations involved. For this reason, numerical methods are used. In the following, the computation technique and the numerical results are presented and discussed.

7.1 Numerical Method

Essentially all definite integrals are evaluated numerically by Simpson's rule. The only exception is the statistical weight g_8 given by Eq. 6.28 which can be simplified analytically to an expression in terms of the error function. The relevant equation for this derivation is Eq. A.3, provided in Appendix A.

When Simpson's rule is applied, an initial and arbitrary number of equally-spaced increments of the dummy variable of integration are selected to perform a numerical integration. Then, the computation is repeated by using twice the number of increments. In other words, the size of each increment is reduced by one half. This procedure is repeated until the termination criterion is reached. The termination criterion applied here

is that the errors between consecutive computations do not exceed one percent. It is found that a sufficient number of increments required to produce a satisfactory solution varies from 100 to 400.

7.2 Numerical Data

Experimental data from the open literature have been used for comparison with the numerical results predicted by the Boltzmann statistics-based models. Only those experiments conducted in a vacuum environment with the necessary topographic parameters measured and reported are included for comparison. The surface characteristics and the sources of reference for all the selected data are summarized in Table 7.1.

Since the surface slope is not commonly reported in the literature, only eleven sets of qualifying data are found useful and they cover a wide range of surface roughness and material properties. The specimens include Stainless Steels 303, 304, and 416, Nickel 200, Zirconium-2.5wt% Nb, and Zircaloy-4 and the surface roughness varies from 0.338 μm (smooth) to 9.86 μm (rough). The results are plotted in Figs. 7.1 through 11.

Useful experimental data to assess the accuracy of the spherical models is even scarcer. Measurements of both the thermal contact conductance and the moments of power spectral density are found only in the study by McWaid and Marschall [24]. The specimens tested were made of Aluminum alloy 6061 and Stainless Steel 304 with two types of finishes: bead-blasted and ground. The four sets of data provided by this

Table 7.1 Experiments for thermal contact conductance of nominally-flat surfaces in a vacuum environment

Data/ Figure	Specimen	σ [μm] (μin)	m	m_{0_1} [μm^2]	m_{0_2}	m_{0_4} [$10^{-3}\mu\text{m}^2$]	H [kpsi] (GPa)	E [Mpsi] (GPa)	ν	$\frac{k}{(\text{W/mK})}$	Ref.
1/7.1	SS 303	2.64 (104)	0.1500				2.28 (330)	183 (26.5)	0.30	17.3 (120)	[39]
2/7.2	SS 303	5.92 (233)	0.0998				2.28 (330)	183 (26.5)	0.30	17.3 (120)	[39]
3/7.3	SS 416	3.04 (120)	0.102				2.62 (380)	193 (28.0)	0.30	25.3 (175)	[40]
4/7.4	Ni 200	0.43 i	0.0778				3.67	207	0.30	75.1	[31]
5/7.5	Ni 200	9.86	0.165				2.17	207	0.30	75.1	[31]
6/7.6	SS 304	0.338	0.0509				4.11	207	0.30	19.3	[31]
7/7.7	SS 304	7.74	0.134				2.51	207	0.30	18.9	[31]
8/7.8	Zirconium	0.652	0.0587				3.14			19.8	[31]
9/7.9	Zirconium	6.23	0.141				2.17			20.0	[31]
10/7.10	Zircaloy-4	0.431	0.0346							16.6	[31]
11/7.11	Zircaloy-4	5.60	0.146				2.32			17.2	[31]
12/7.12	Al 6061-T6		3.41	0.0261	1.46		67	0.33	200		[24]
13/7.13	SS 304		0.383	0.00467	0.325	2.93	207	0.30	16		[24]
14/7.14	SS 304		0.507	0.00370	0.515	2.93	207	0.30	16		[24]
15/7.15	SS 304		0.351	0.00124	0.112	2.93	207	0.30	16		[24]

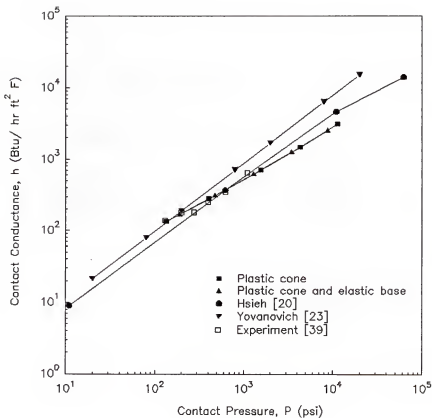


Fig. 7.1 Thermal contact conductance versus contact pressure for Stainless Steel 303 surfaces in a vacuum (Data 1)

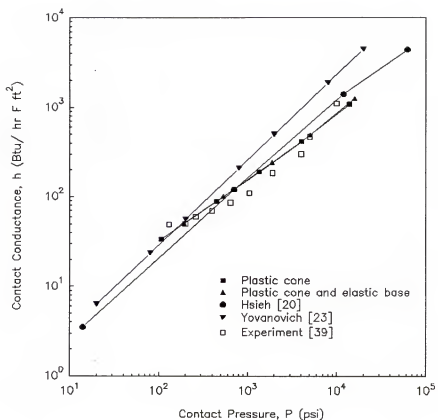


Fig. 7.2 Thermal contact conductance versus contact pressure for Stainless Steel 303 surfaces in a vacuum (Data 2)

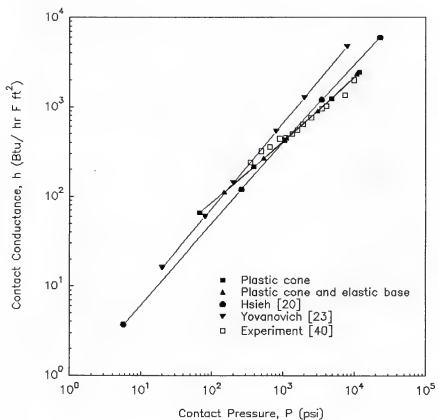


Fig. 7.3 Thermal contact conductance versus contact pressure for Stainless Steel 416 surfaces in a vacuum (Data 3)

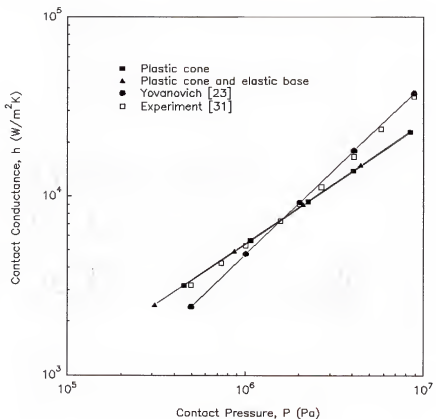


Fig. 7.4 Thermal contact conductance versus contact pressure for Nickel 200 surfaces in a vacuum (Data 4)

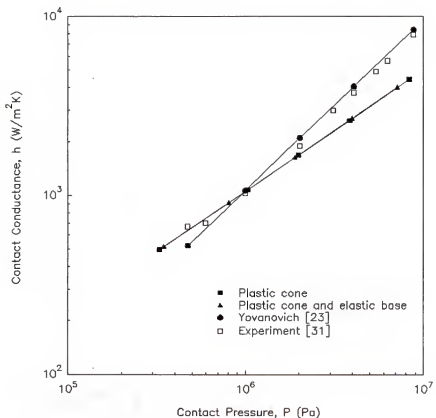


Fig. 7.5 Thermal contact conductance versus contact pressure for Nickel 200 surfaces in a vacuum (Data 5)

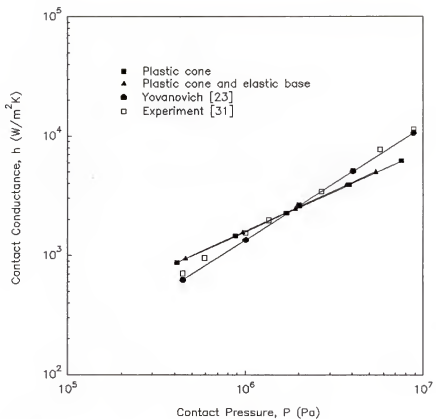


Fig. 7.6 Thermal contact conductance versus contact pressure for Stainless Steel 304 surfaces in a vacuum (Data 6)

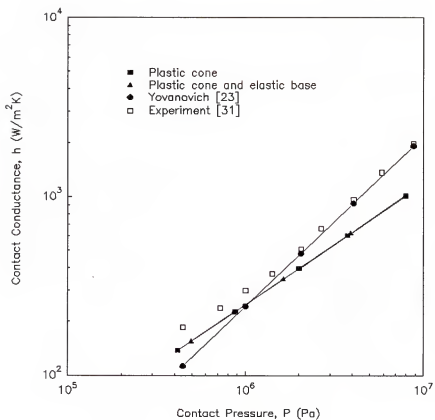


Fig. 7.7 Thermal contact conductance versus contact pressure for Stainless Steel 304 surfaces in a vacuum (Data 7)

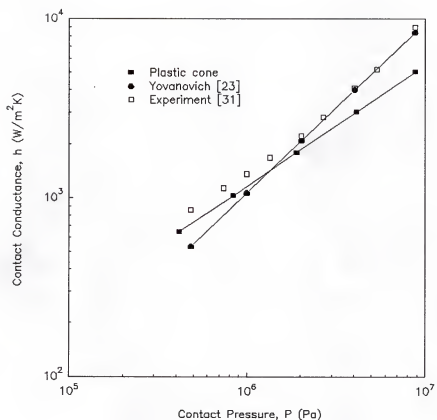


Fig. 7.8 Thermal contact conductance versus contact pressure for Zirconium-2.5%wt Nb surfaces in a vacuum (Data 8)

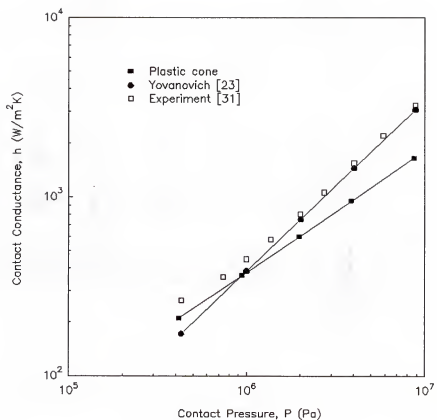


Fig. 7.9 Thermal contact conductance versus contact pressure for Zirconium-2.5%wt Nb surfaces in a vacuum (Data 9)

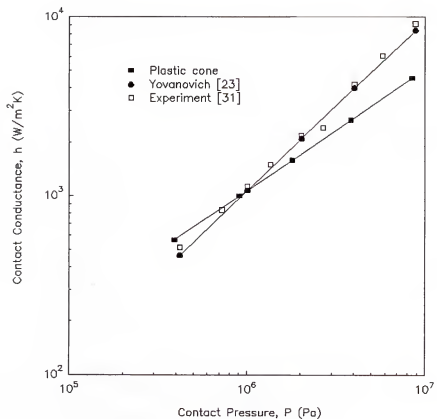


Fig. 7.10 Thermal contact conductance versus contact pressure for Zircaloy-4 surfaces in a vacuum (Data 10)

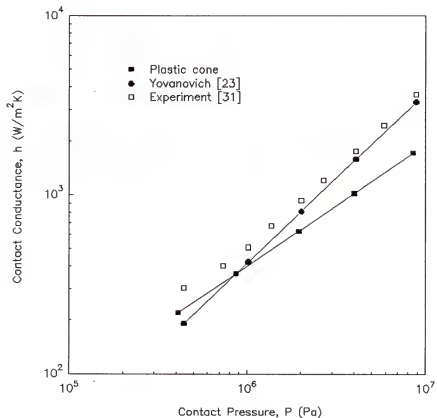


Fig. 7.11 Thermal contact conductance versus contact pressure for Zircaloy-4 surfaces in a vacuum (Data 11)

reference are used to validate the spherical models. The test results of the bead-blasted surfaces are presented in Figs. 7.12 and 13. Tests of the contact between the ground surfaces oriented with lays parallel and perpendicular to each other are plotted in Figs. 7.14 and 15, respectively. It should be noted that these figures (Figs. 7.1 through 15) also include the predictions made by others as reported in the literature (Section 3.2).

A dimensionless plot, Fig. 7.16, using parameters derived in the previous correlation studies [19,29], further compares the prediction by the plastic cone model and the first eleven sets of the experimental data listed in Table 7.1. In this comparison, the data are plotted in dimensionless contact conductance,

$$h^* = \frac{h \sigma}{mk}$$

versus the dimensionless pressure,

$$P^* = \frac{P}{H}$$

Elastic deformation is accounted for in the other three Boltzmann statistics-based models (plastic cone and elastic base, elastic spherical asperity, elastic and plastic spherical asperity). This leads to the presence of the modulus of elasticity and the Poisson ratio in the analysis. A dimensionless plot becomes inappropriate in such models.

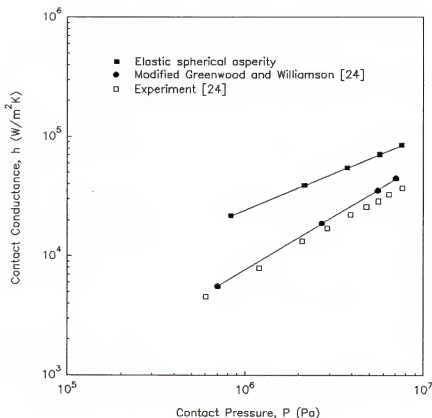


Fig. 7.12 Thermal contact conductance versus contact pressure for Aluminum 6061-T6 surfaces in a vacuum (Data 12)

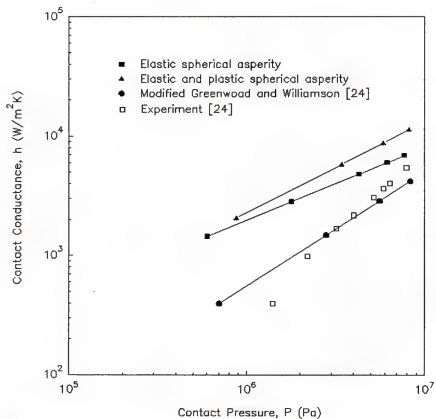


Fig. 7.13 Thermal contact conductance versus contact pressure for Stainless Steel 304 surfaces in a vacuum (Data 13)

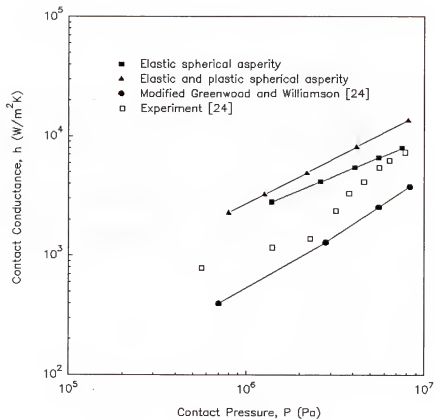


Fig. 7.14 Thermal contact conductance versus contact pressure for Stainless Steel 304 surfaces in a vacuum (Data 14)

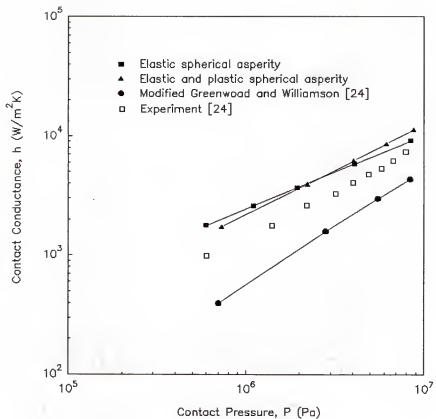


Fig. 7.15 Thermal contact conductance versus contact pressure for Stainless Steel 304 surfaces in a vacuum (Data 15)

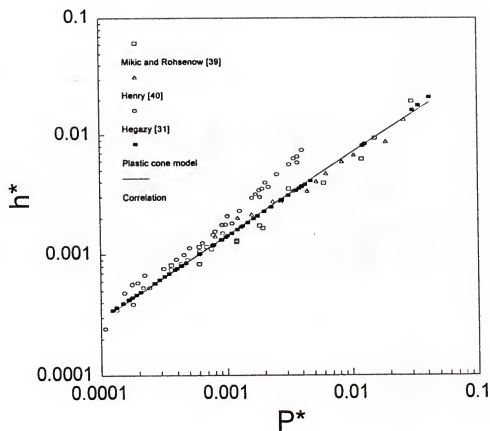


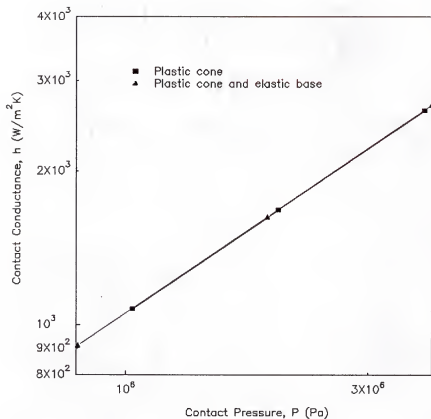
Fig. 7.16 Dimensionless thermal contact conductance versus dimensionless contact pressure

7.3 Discussion

The numerical results by the conical models are compared to the contact conductance data measured by Mikic and Rohsenow [39] and Henry [40] in Figs. 7.1, 2, and 3. The difference between the predicted and the empirical values is within 30%. The predictions by the Hsieh model and the Yovanovich model are also presented in these three figures. In Fig. 7.1, the Yovanovich model overpredicts the contact conductance while the Hsieh model and the conical models are in good agreement with the experimental data. However, in Figs. 7.2 and 3, the conical models are found to be the best among them.

The experiments conducted by Hegazy [31] are presented in Figs. 7.4 through 11. Here, the trend observed is consistent in that the predictions by the conical models agree well with the experiment at low loading pressures. As the pressure increases, the models underpredict the contact conductance. A comparison with the Yovanovich model indicates that the conical models work better at low loading pressures while the Yovanovich model works better at high loading pressures.

It is found that the predicted values of the thermal contact conductance by the plastic cone and elastic base model are consistently higher than those by the plastic cone model. As the two predictions are very close, some numerical data are plotted again with an enlarged scale in Fig. 7.17 to illustrate the claim. This phenomenon is explained by the fact that the elastic base deflection of a load carrying asperity is considered in the plastic cone and elastic base model. Thus, for a given contact pressure, even though the total



a) Data 5 ($E/H = 95.4$)

Fig. 7.17 Thermal contact conductance versus contact pressure for a) Data 5 and b) Data 6

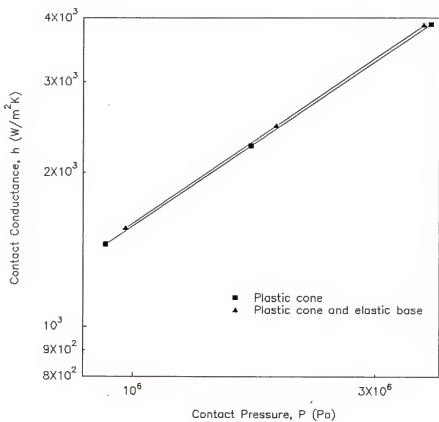
b) Data 6 ($E/H = 50.4$)

Fig. 7.17 -- continued

actual contact area is the same, more contact spots are formed as illustrated in Fig. 7.18. Hence, the resultant conductance is higher.

One expects that if the modulus of elasticity, E , is large, its effect on the prediction of contact conductance would be small as a result of the small base deflection. This variation can be found in the numerical results. Among all the data presented in Fig. 7.1 through Fig. 7.7, the two extreme values of the ratio E/H are 95.4 and 50.4 for Data 5 and Data 6, respectively. The plots in Figs. 7.17a and 17b, set up in the same scale, indicate that the smaller the E/H is, the larger the difference between the two predictions is. Thus, the numerical results agree with the physical expectation.

In Figs. 7.12 and 13, the predictions by the spherical models are compared to the empirical data obtained from the tests of bead-blasted aluminum and stainless steel surfaces. The disagreement is found to be large. However, the modified Greenwood and Williamson model, also using spherical asperities, appears to be satisfactory in predicting the contact conductance.

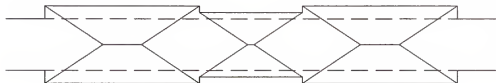
The comparisons for the ground surfaces are presented in Figs. 7.14 and 15. As the surfaces are strongly anisotropic, the equivalent values of the spectral moments given by McWaid and Marschall [24] are used in the prediction. Again, the present spherical models overpredict the contact conductance in all cases tested.

The elastic asperity model tends to predict a lower conductance than the elastic and plastic asperity model at high contact pressure as shown in Figs. 7.13 to 15. This can be ascribed to the fact that at high pressure many touching asperities should be deformed plastically while the elastic spherical asperity model still analyzes the contact by

a) Plastic cone model



b) Plastic cone and elastic base model



Same total contact area
but more contact spots

Fig. 7.18 Illustration of the difference in deformation of asperities for a given contact pressure between a) the plastic cone model and b) the plastic cone and elastic base model

considering the asperities in elastic deformation. The stress-strain diagrams given in Fig. 7.19 provide the basis that less contact area is predicted by the elastic spherical asperity model at high contact pressure. As a result, the estimates of the thermal contact conductance are low.

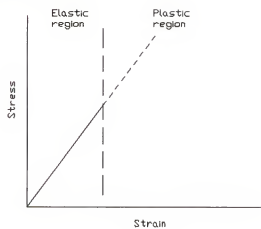
The dimensionless plot given in Fig. 7.16 effectively summarizes the data discussed in this chapter. Here, all the predictions by the plastic cone model are plotted. The correlation between the predicted h^* and P^* is expressed by

$$h^* = 0.170 P^{0.693} \quad (7.1)$$

The good agreement ($\pm 30\%$) between the prediction by the plastic cone model and the measurements by Mikic and Rohsenow [39] and Henry [40] spans a wide range of P^* ($4 \times 10^{-4} < P^* < 3 \times 10^{-2}$). For Hegazy's [31] experiments, good agreement ($\pm 30\%$) is found when P^* is less than 6×10^{-4} . When P^* is greater than 6×10^{-4} , the model tends to underpredict and the deviation increases with P^* . The worst case found is at P^* approximately equal to 4×10^{-3} , where the experimental h^* is twice as high as the predicted h^* .

On the basis of the above analysis, the predictions of thermal contact conductance by the conical models at low loads ($P^* < 6 \times 10^{-4}$) are highly reliable. At high load, since there is a large deviation among existing empirical data, it is difficult to assess the accuracy of the predicting models. Nonetheless, the predictions by the conical models are within the uncertainty in the experimental data.

a) Elastic model



b) Elastic and plastic model

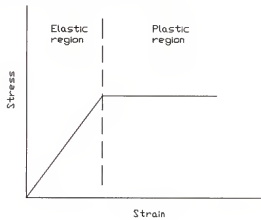


Fig. 7.19 Stress-strain analyses used by the two spherical asperity models:
a) elastic model and b) elastic and plastic model

In summary, the Boltzmann statistical model is found to perform well with the assumptions made in the two conical models. The deviation between their predictions are negligibly small for all the cases tested. In addition, the consideration of the elastic base deformation complicates the computation and that costs a longer computer time to obtain a numerical solution. Thus, it is concluded that the plastic cone model is the most effective among all the Boltzmann statistics-based models developed in this investigation.

CHAPTER 8

MEASUREMENT OF ELECTRICAL CONTACT CONDUCTANCE

Experiments were conducted in order to provide additional data to evaluate the accuracy of the Boltzmann statistics-based models in the prediction of the contact conductance. However, instead of measuring the thermal contact conductance, which requires a costly apparatus, the electrical contact conductance was measured as the two conductances appear to be analogous.

Some investigators have studied the electrical contact conductance between metals, such as silver, aluminum, copper, low carbon steel, iron, among others [41,42]. It has been shown that the surface film on metal, such as oxide layer, yields unnoticeable effect on the thermal conductance yet reduces the electrical conductance considerably. For this reason, stainless steel was chosen to be the test material as it is highly resistant to corrosion. Moreover, the low electrical conductivity of the stainless steel (approximately $2 \times 10^6 \Omega^{-1}m^{-1}$) is advantageous from the standpoint that the minute voltage drop across the contact interface can be more sensitively measured by instruments. The details of the experimental procedures and the test results are given below.

8.1 Surface Preparation and Measurement

Two sets of stainless steel specimens (a pair in each set) were prepared with different surface textures. Each specimen was cut from a 25 mm diameter Stainless Steel 304 bar stock and then machined down to 19 mm long by milling and turning. Its surfaces were lapped with a 600 grit compound to reduce waviness. The flatness measurement was made by using a 20 mm surface profile trace drawn by a Dektak profilometer. It was found that the surface was originally spherical in shape with the center being higher. The waviness readings from the peak to the valley were greater than 1 μm . In order to reduce this waviness, the lapping technique used to produce gauge blocks was applied. In this technique, a set of three surfaces were lapped against each other (two at a time) alternately and repeatedly with fine lapping compounds (800 grit, 1000 grit, and 1200 grit successively). The surfaces were measured again and found that the flatness was improved to a waviness height of less than 0.7 μm .

Surfaces were roughened by sandblasting with beads of sizes between 0.5 and 0.8 mm. The specimen was placed 20 cm away from the nozzle of the blasting gun. The desirable roughness was accomplished by adjusting the blaster pressure (60 psi for rough surfaces and 40 psi for smooth surfaces). Each surface was sandblasted until a homogeneous texture was found under a microscope. The total time required for this blasting process was about 15 seconds.

The processed surfaces were then cleaned ultrasonically with detergent solution, acetone, and distilled water successively. Again, for each surface two 20 mm profiles

perpendicular to each other were recorded by a Dektak profilometer (see figures in Appendix B). In these recorded profiles, the waviness to roughness ratio is found to be small to the extent that the surface waviness is negligible. The root-mean-square roughness of the surface was measured by a Brush profilometer and their values are summarized in Table 8.1.

8.2 Apparatus Setup and Data Collection

The material properties of the stainless steel bar stock had been measured before the electrical contact conductance was tested. The Vickers hardness number was found to be 299 (425 kpsi) by a Buchler Micromet II microhardness tester. The electrical conductivity of the steel was measured by a setup illustrated in Fig. 8.1. Here, a 1.2-V, 40 amp hour battery was used to produce a 1 A current during the test. The electrodes were attached to the stainless steel bar by means of a brass ring where three screws are provided as shown in Fig. 8.2. The voltage drop across the electrodes separated by a distance L was of the order of $10 \mu\text{V}$, which is too small for conventional voltmeters to measure. Therefore, a Keithley Model 182 digital voltmeter ($0.01 \mu\text{V}$ resolution) was used. The measured resistance R_e versus the separation, L , and a linear regression line are plotted as shown in Fig. 8.3. The slope of the line was determined to be $1.47 \times 10^{-3} \Omega\text{m}^{-1}$, which yields an electrical conductivity of $1.34 \times 10^6 \Omega^{-1}\text{m}^{-1}$. The linear relationship among the data points also indicates the reliability of this techniques in measuring low resistance.

Table 8.1 Summary of surface roughness

		Root-mean-square roughness		
		low (μm)	high (μm)	average (μm)
Set 1	Specimen A	1.372	1.473	1.423
	Specimen B	1.143	1.473	1.308
Set 2	Specimen C	0.8636	1.016	0.9398
	Specimen D	0.6604	0.8128	0.7366

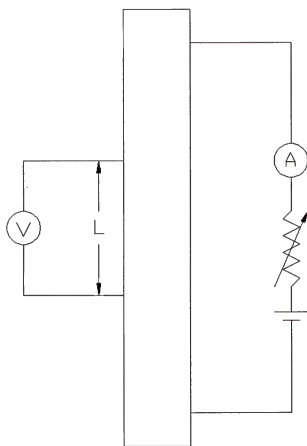
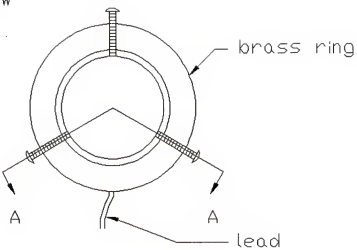


Fig. 8.1 Schematic of electrical conductivity measurement

Top view



Side view (Section A-A)

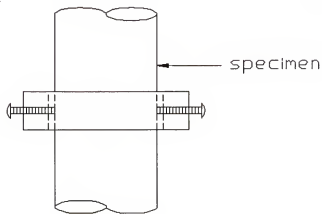


Fig. 8.2 Connection of an electrode to a specimen

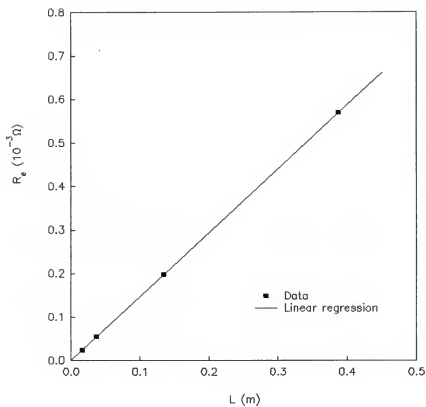


Fig. 8.3 Measured resistance of stainless steel bar stock versus length

A test rig was designed for the measurement of the electrical contact conductance as depicted in Fig. 8.4. The features of this setup are analogous to those of the schematic for a thermal test shown in Fig. 3.9. The electrodes were attached to the copper bars and the stainless steel specimens in the same manner as before (Fig. 8.2). The copper was chosen for its softness and high electrical conductivity. It allows the current to flow uniformly through the specimens. The stack was placed between two platforms of a hydraulic press. At the top end of the stack, the test pressure was monitored by means of a load cell constructed and calibrated by the Civil Engineering Department of the College of Engineering of the University of Florida. A ball bearing was also used such that any misalignment of the stack would not disturb the loading at the interface. Finally, insulators were used so that the current would not be channeled through the hydraulic press.

During the test the rheostat was adjusted to maintain a 1 A current in the circuit. Every time the load was changed, a waiting period of ten minutes was scheduled to allow the instrument readings to stabilize. Then, the voltage drop V across the contact interface, the current I , and the load cell signal were recorded.

The measured resistance $R_{e,meas}$, equal to V/I , includes both the contact resistance $R_{e,com}$ and the bulk resistance $R_{e,bulk}$. Then, the contact resistance is obtained by using the formula

$$R_{e,com} = R_{e,meas} - R_{e,bulk} \quad (8.1)$$

where

$$R_{e,meas} = \frac{V}{I}$$

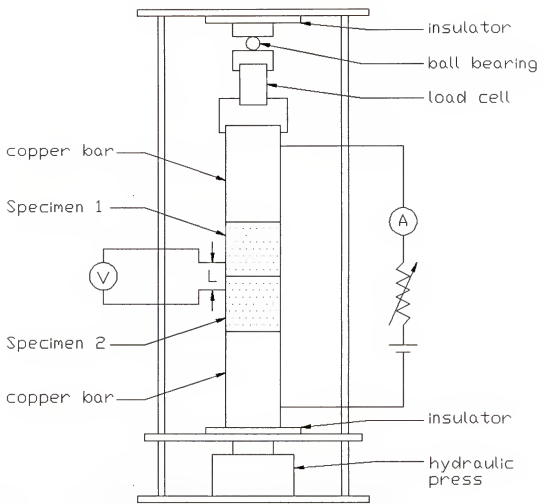


Fig. 8.4 Schematic of the apparatus for testing electrical contact conductance

and

$$R_{e,bulk} = \frac{L}{kA}$$

The corresponding contact conductance per unit area is

$$h_e = \frac{1}{R_{e,conf} A} \quad (8.2)$$

The empirical results are plotted and discussed in the following section.

8.3 Empirical Results and Discussion

The measured values of the electrical contact conductance are presented in Figs. 8.5 and 6. The major source of error is the uncertainty in the measurement of L , which is used to determine $R_{e,bulk}$. As h_e is related to $R_{e,bulk}$ by Eqs. 8.1 and 2, the magnitude of the error increases with the applied load.

The experimental results are compared to the prediction by the plastic cone model as it was found to be the most satisfactory among all the Boltzmann statistics-based models. It is found that the measured values of the electrical contact conductance are considerably lower than the predicted values by Eq. 6.33. A correction factor λ_e is introduced to improve the predicted values and the results are plotted with the experimental data. The values of λ_e are 0.0302 and 0.0704 for the sets 1 and 2, respectively.

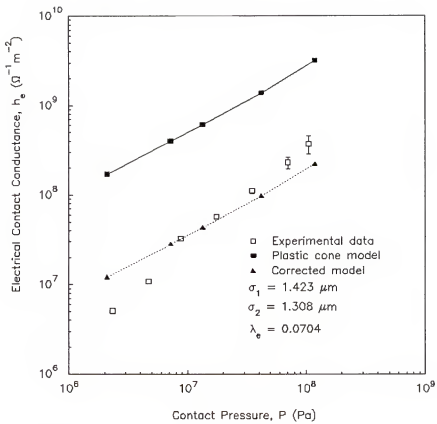


Fig. 8.5 Electrical contact conductance versus contact pressure for Stainless Steel 304 surfaces (Set 1)

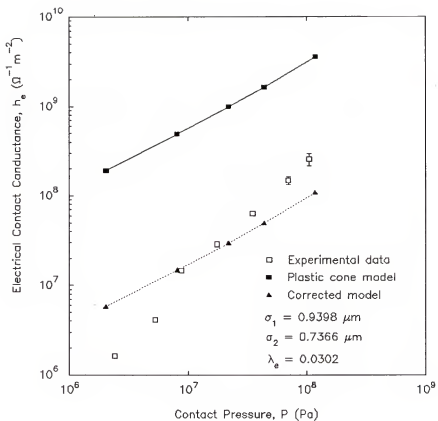


Fig. 8.6 Electrical contact conductance versus contact pressure for Stainless Steel 304 surfaces (Set 2)

One can observe that the measured electrical contact conductance increases as the surface roughness increases. This phenomenon, also reported in references [42,43], is in contrast with the traditional relationship between the contact conductance and the surface roughness because of the presence of surface films. In the experiment by Tsukizoe and Hisakado [42], both electrical and thermal contact conductances were tested. The lowest and highest values of the dimensionless electrical-to-thermal ratio, equivalent to λ_c presented here, for a contact between copper surfaces was found to be 0.0476 for smooth surfaces and 0.143 for rough surfaces, respectively.

The physical significance of λ_c is related to the effect of the presence of surface film, which is electrically insulating. In general, a metal surface is covered by a composition of tarnish and alien films [44]. A tarnish film, such as an oxide or sulphide, is a film in which one constituent consists of the atoms of the substrate material. An alien film, on the other hand, is formed by substances in the surroundings deposited on a metal surface, for example, water or lubricant film. The surface films permit the flow of phonons but inhibit the flow of electrons. The reason is that the film and the metal have similar thermal conductivities but the electrical conductivity of the film is much lower than that of the metal. For instance, the electrical conductivity of copper oxide is $5 \times 10^3 \Omega^{-1}m^{-1}$ and that of pure copper is $5 \times 10^7 \Omega^{-1}m^{-1}$. Thus, when two surface asperities are in contact, the electrons can be conducted through a portion of the contact spot area only where the surface films are ruptured. This results in a low electrical contact conductance compared to the thermal one.

One surface film rupture mechanism is by asperity penetration as illustrated in Fig. 8.7 [43]. This figure shows that under a given load the sharper asperity (found in a rougher surface) produces a larger pure metal-metal contact area (electrically conductive) but the same load-carrying area (thermally conductive). This explains why the contact conductance decreases with the surface roughness in a thermal test but increases in an electrical test as the values of λ_e are found in Figs. 8.5 and 6.

Another mechanism that induces pure metal-metal contact is by film cracking. Osias and Tripp performed a test modeling a film covered spherical asperity of a metal surface by a plastic sphere coated with a brittle shell [45]. Subsequent to the loading of this sphere, the modes of cracking observed are radial, circumferential, and craze cracks. Thus, in reality electrons can be conducted through these cracks of an insulating film.

If a surface film is sufficiently thin (thickness less than 50 Å), electrons can pass through the film by tunneling effect. In this mechanism, an electron having a potential higher than the work function of the film will jump over the potential barrier. Thus, a flow of electrons is induced.

In this experimental investigation, it is found that the surface film effect on the electrical contact conductance between two stainless steel surfaces is significant. The magnitude of the correction factor, λ_e , is comparable to those found in the literature [42].

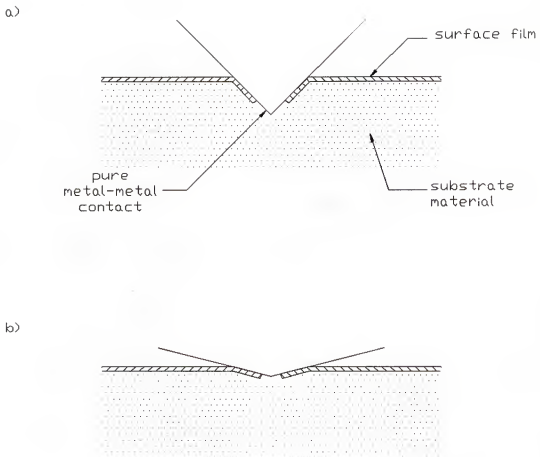


Fig. 8.7 Demonstration of larger pure metal-metal contact area produced by
a) rough surfaces in contact than b) smoother surfaces in contact

CHAPTER 9 CONCLUSIONS AND RECOMMENDATIONS

This investigation has shown that the prediction of thermal contact conductance by statistical mechanics is viable. Considering surface asperities comparable to molecules in the traditional sense of microscopic viewpoint, the Boltzmann statistical model successfully determines the "most probable distribution" of the contact spots. Thus, a relationship between the contact conductance and the relative pressure is derived.

A thorough study was conducted by applying various assumptions of the surface model and the deformation mechanism in conjunction with the computation procedures of the Boltzmann model. It is found that modeling a rough surface by conical asperities whose summits are deformed plastically is the most effective approach. The disagreement between the predicted thermal conductance and the published data is less than 30% when the dimensionless pressure (P/H) is less than 6×10^{-4} . Over the entire test domain, the worst empirical data is twice as much as the prediction.

The results of the models using spherical asperities are less accurate. However, the prediction by the elastic and plastic spherical asperity model gives a trend that is comparable to the experimental data.

The differences in the predictions by the four Boltzmann statistics-based models developed agree with the expectations. For instance, due to the base deformation mechanism, the plastic cone and elastic base model predicts a thermal contact conductance

that is higher than the plastic cone model. Moreover, the elastic spherical asperity model predicts a conductance that is lower than the elastic and plastic asperity model. This is because the former overestimates the stress on a contact under high load.

A number of recommendations are suggested to explore this approach further in the future. First, the statistical weight function, g_s , is defined on the basis of the base plane separation, ξ , varying between 0 and 16σ (2 times the highest asperity). In reality, if ξ becomes less than a critical value ξ_c , mechanical failure of the bulk materials occurs. Thus, it is more reasonable that ξ varies between ξ_c and 16σ . The value of ξ_c can be determined by the existing models that relate ξ and the loading pressure. Candidate models include the Hsieh model [20] and the modified Greenwood and Williamson model [24].

The Boltzmann statistical model has been explored in this investigation and reasonably accurate predictions are obtained. The Bose-Einstein and Fermi-Dirac statistical models, assuming that the particles are indistinguishable, have been applied successfully in statistical thermodynamics. Thus, these two models may also play an important role in the field of contact conductance. Investigations of these two statistical models are recommended.

A correlation among the numerical results of the contact conductance and the parameters involved is also encouraged. A successful correlation should simplify the complicated numerical integrations.

The experimental results of this research show that the presence of electrically insulating surface films significantly reduce the pure metal-metal contact area between the

stainless steel surfaces. The film effect results in a low measured electrical contact conductance. Film penetration and film cracking are the fundamental mechanisms that produce pure metal-metal contacts, where the electrons are easily transferred. The electrons can also be transferred by the tunneling effect if the film is sufficiently thin. At the present time, the models that predict the film effect partially depend on experimental measurements.

Still, testing contact conductance electrically plays a vital role in the field of thermal contact conductance. The main reason is the cost of a test facility being exceedingly low. In addition, testing electrically is much less time-consuming as the steady state can be reached rapidly. In order to make this measurement useful, the selection of test materials is critical. The specimens should not be chemically active at room temperature. In this regard, good candidates include gold and platinum.

REFERENCES

1. Goswami, D.Y., Hsieh, C.K., Klausner, J.F., Jotshi, C.K., Kumar, M.K., Malakar, S.M. and Leung, M., "Development of an Advanced Storage Electric Water Heater," Final Report-Phase III, No. UFME/SEECL-9501, for the Department of Energy and Florida Power and Light Co. by the Solar Energy and Energy Conversion Laboratory, Gainesville, FL, January 1995.
2. Skipper, R.G.S. and Wootton, K.J., Thermal Resistance Between Uranium and Can, Proceedings of the 2nd International Conference on Peaceful Uses of Atomic Energy, Geneva, Paper P/87, Sep. 1958.
3. Fried, E. and Costello, F.A., "Interface Thermal Contact Resistance Problem in Space Vehicles," ARS Journal, Feb. 1962, pp. 273-243.
4. Fisher, N.J. and Yovanovich, M.M., "Thermal Constriction Resistance of Sphere/Layered Flat Contacts: Theory and Experiment," ASME, Journal of Heat Transfer, Vol. 111, May 1989, pp. 249-256.
5. Phelan, P.E., Song, Y., Nakabeppu, O., Ito, K., Hijikata, K., Ohmori, T., and Torikoshi, K., "Film/Substrate Thermal Boundary Resistance for an Er-Ba-Cu-O High-T_c Thin Film," ASME, Journal of Heat Transfer, Vol. 116, Nov. 1994, pp. 1038-1041.
6. Sommers, R.R., II, Fletcher, L.S., Flack, R.D., "Explanation of Thermal Rectification," AIAA Journal, Vol. 25, No. 4, Apr. 1987, pp. 620-621.
7. Stevenson, P.F., Peterson, G.P., and Fletcher, L.S., "Thermal Rectification in Similar and Dissimilar Metal Contacts," ASME, Journal of Heat Transfer, Vol. 113, Feb. 1991, pp. 30-36.
8. Antonetti, V.W and Yovanovich, M.M, "Enhancement of Thermal Contact Conductance by Metallic Coatings: Theory and Experiment," ASME, Journal of Heat Transfer, Vol. 107, Aug. 1985, pp. 513-519.
9. Peterson, G.P., Fletcher, L.S., "Measurement of the Thermal Contact Conductance and Thermal Conductivity of Anodized Aluminum Coatings," ASME, Journal of Heat Transfer, Vol. 112, Aug. 1990, pp. 579-585.

10. Fenech, H. and Rohsenow, W.M., Thermal Conduction of Metallic Surfaces in Contact, Report No. NYO-2136, for the United States Atomic Energy Commission by Heat Transfer Laboratory, M.I.T., Cambridge, MA, May 1959.
11. Bejan, A., Heat Transfer, John Wiley & Sons, Inc., New York, 1993.
12. Lee, J.F., Sears, F.W., and Turcotte, D.L., Statistical Thermodynamics, Addison-Wesley, Inc., Reading, MA, 1963.
13. Hsieh, C.K. and Davis, F.F., "Bibliography on Thermal Contact Conductance," AFML-TR-69-24, Air Force Material Laboratory, Mar. 1969.
14. Snaith, B., Probert, S.D., and O'Callaghan, P.W., "Thermal Resistances of Pressed Contacts," Applied Energy, Vol. 22, 1986, pp. 31-84.
15. Madhusudana, C.V., and Fletcher, L.S., "Contact Heat Transfer - The Last Decade," AIAA Journal, Vol. 24, No. 3, Mar. 1986, pp. 510-523.
16. Fletcher, L.S., "Recent Developments in Contact Conductance Heat Transfer," ASME, Journal of Heat Transfer, Vol. 110, Nov. 1988, pp. 1059-1070.
17. Holm, R., Electric Contacts, Gebers, Stockholm, 1946, pp. 1-23.
18. Gibson, R.D., "The Contact Resistance for a Semi-infinite Cylinder in a Vacuum," Applied Energy, Vol. 2, 1976, pp. 57-65.
19. Cooper, M.G., Mikic, B.B., Yovanovich, M.M., "Thermal Contact Conductance," International Journal of Heat and Mass Transfer, Vol. 12, 1969, pp. 279-300.
20. Hsieh, C.K., Correlation and Prediction of Thermal Contact Conductance for Nominally Flat Surfaces, Ph.D. Thesis, Purdue University, West Lafayette, IN, Jun. 1968.
21. Hsieh, C.K., "A Critical Evaluation of Surface Geometrical Parameters For a Nominally Flat Surface Model," ASME, Journal of Lubrication Technology, Vol. 96, Oct 1974, pp. 638-639.
22. D'yachenko, P.E., Tolkacheva, N.N., Andreev, G.A., and Karpova, T.M., The Actual Contact Area between Touching Surfaces, Consultants Bureau, New York, 1964.

23. Yovanovich, M.M., "Thermal Contact Correlations," *Spacecraft Radiative Transfer and Temperature Control*, Horton, T.E., ed., AIAA, *Progress in Astronautics and Aeronautics*, Vol. 83, New York, 1982, pp. 83-95.
24. McWaid, T. and Marschall, E., "Thermal Contact Resistance across Pressed Metal Contacts in a Vacuum Environment," *International Journal of Heat Mass Transfer*, Vol. 35, No. 11, 1992, pp. 2911-2920.
25. Greenwood, J.A. and Williamson, J.B.P., "Contact of Nominally Flat Surfaces," *Proceedings of the Royal Society, London*, Vol. 295, Series A, 1966, pp. 300-319.
26. Timoshenko, S. and Goodier, J.N., *Theory of Elasticity*, 2nd ed., McGraw-Hill, Inc., 1951.
27. Tabor, D., *The Hardness of Metals*, Oxford University Press, New York, 1951.
28. Miller, R.G and Fletcher, L.S., "A Facility for the Measurement of Thermal Contact Conductance," *Southern Seminar on Thermal Science*, 10th, Proc, New Orleans, La, Apr 11-12 1974, published by Tulane Univ., Dep. of Mech. Eng., New Orleans, pp. 263-285.
29. Tien, C.L., "A Correlation for Thermal Contact Conductance of Nominally-Flat Surface in a Vacuum," *Proceeding of the 7th Thermal Conductivity Conference*, U.S. Bureau of Standards, 1968, pp. 755-759.
30. Veziroglu, T.N., "Correlation of Thermal Contact Conductance Experimental Results," *Thermophysics of Spacecraft and Planetary Bodies*, Heller, G.B. ed., AIAA, *Progress in Astronautics and Aeronautics*, Vol. 20, New York, 1967, pp. 879-899.
31. Hegazy, A.A, *Thermal Joint Conductances of Conforming Rough Surfaces: Effects of Surface Microhardness Variation*, Ph.D. thesis, Department of Mechanical Engineering, University of Waterloo, Ontario, 1985.
32. Antonetti, V.W. and Whittle, T.D., "An approximate Thermal Contact Conductance Correlation," *ASME, Experimental/Numerical Heat Transfer in Combustion and Phase Change*, Vol. 170, 1991, pp. 35-42.
33. Sonntag, R.E and Van Wylen, G.J., *Fundamentals of Statistical Thermodynamics*, John Wiley and Sons, Inc., New York, 1966.

34. Williamson, J.B.P., "Microphotography of Surfaces," Proceedings of the Institution of Mechanical Engineers, Vol. 182, Pt.3K, 1967-68, pp. 21-30.
35. Williamson, J.B.P., "The Shape of Solid Surfaces," Surface Mechanics, Proceedings of the ASME Annual Winter Meeting, Los Angeles, CA, Nov. 1969, pp. 24-35.
36. Nayak, P.R., "Random Process Model of Rough Surfaces," ASME, Journal of Lubrication Technology, Vol. 93, Jul. 1971, pp. 398-407.
37. Bush, A.W., Gibson, R.D., and Keogh, J.P., "The Limit of Elastic Deformation in the Contact of Rough Surfaces," Mech. Res. Commun., Vol. 3, 1976, pp. 169-174.
38. McCool, J.I., "Comparison of Models for the Contact of Rough Surfaces," Wear, Vol. 107, 1986, pp. 37-60.
39. Mikic, B.B. and Rohsenow, W.M., "Thermal Contact Resistance," Rep. No. 4542-41, M.I.T., Cambridge, MA, 1966.
40. Henry, J.J., Thermal Contact Resistance, A.E.C. Rep. No. 2079-2, M.I.T., Cambridge, MA, 1964.
41. Tsukizoe, T. and Hisakado, T., "On the Mechanism of Heat Transfer between Metal Surfaces in Contact, Part 1: Theoretical Analysis and Experimental Justification of Theory," Heat Transfer-Japanese Research, Vol. 1, No. 1, Jan.-Mar. 1972, pp. 104-112.
42. Tsukizoe, T. and Hisakado, T., "On the Mechanism of Heat Transfer between Metal Surfaces in Contact (2nd Report, Thermal Contact Resistance between Metal Surfaces in Vacuum)," Heat Transfer-Japanese Research, Vol. 1, No. 2, Apr.-Jun. 1972, pp. 23-31.
43. Braunovic, M., "Aluminum Connections: Legacies of the Past," Electrical Contacts-1994, Proceedings of the 4th IEEE Holm Conference on Electrical Contacts, Chicago, IL, Oct. 1994, pp. 1-31.
44. Holm, R., Electric Contacts Theory and Application, 4th ed., Springer-Verlag, New York, 1981.
45. Osias, J.R. and Tripp, J.H., "Mechanical Disruption of Surface Films on Metals," Wear, Vol. 1966, pp. 388-397.

APPENDIX A MATHEMATICAL EQUATIONS

Probability density function,

$$f(x) = \frac{1}{\sqrt{2\pi}\sigma} e^{-\frac{1}{2}\left(\frac{x-\mu}{\sigma}\right)^2} \quad (\text{A.1})$$

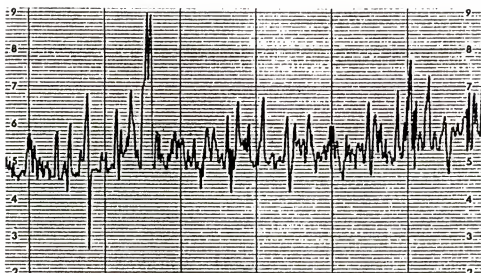
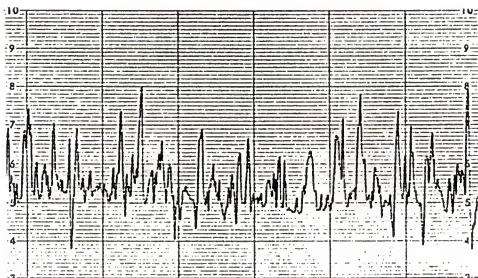
Error function,

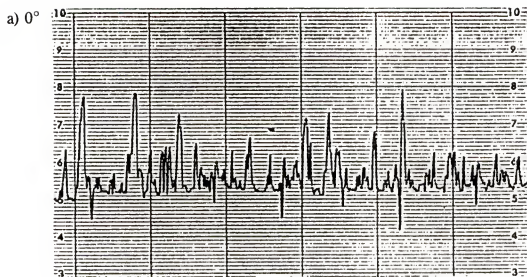
$$\text{erf}(z) = \frac{2}{\sqrt{\pi}} \int_0^z e^{-\xi^2} d\xi \quad (\text{A.2})$$

Integration of relevant exponential function,

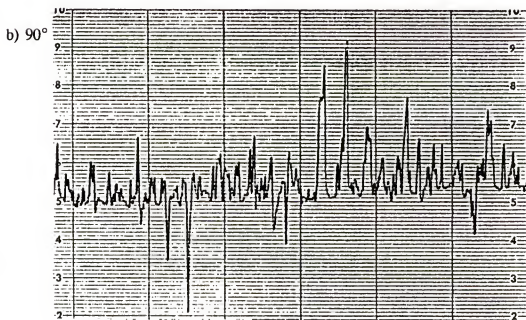
$$\begin{aligned} \int_a^b e^{-Ax} e^{-Bx^2} x^2 dx &= -\frac{1}{2B} \left\{ x e^{-Ax} e^{-Bx^2} \Big|_a^b - \frac{A}{2B} e^{-Ax} e^{-Bx^2} \Big|_a^b \right. \\ &\quad \left. + \left(-\frac{A^2}{2B} - 1 \right) \frac{\sqrt{\pi} e^{-\frac{A^2}{4B}}}{2\sqrt{B}} \left[\text{erf} \left(\sqrt{B}x + \frac{A}{2\sqrt{B}} \right) \right]_a^b \right\} \end{aligned} \quad (\text{A.3})$$

APPENDIX B
RECORDED SURFACE PROFILES

a) 0° Vertical scale: $2\mu\text{m}/\text{DIV}$ Horizontal scale: $0.1\text{cm}/\text{DIV}$ b) 90° Vertical scale: $2\mu\text{m}/\text{DIV}$ Horizontal scale: $0.1\text{cm}/\text{DIV}$ Fig. B.1 Recorded surface profiles of Specimen A: a) 0° and b) 90°

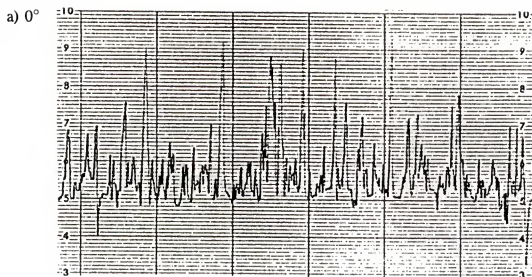


Vertical scale: $2\mu\text{m}/\text{DIV}$ Horizontal scale: $0.1\text{cm}/\text{DIV}$

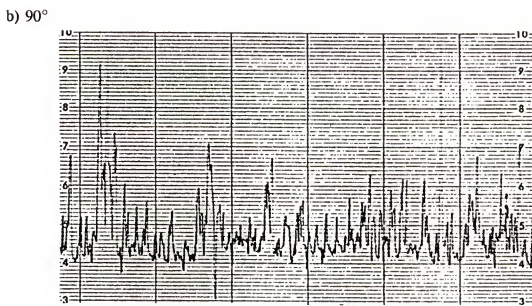


Vertical scale: $2\mu\text{m}/\text{DIV}$ Horizontal scale: $0.1\text{cm}/\text{DIV}$

Fig. B.2 Recorded surface profiles of Specimen B: a) 0° and b) 90°

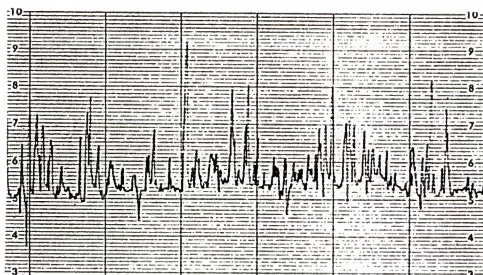
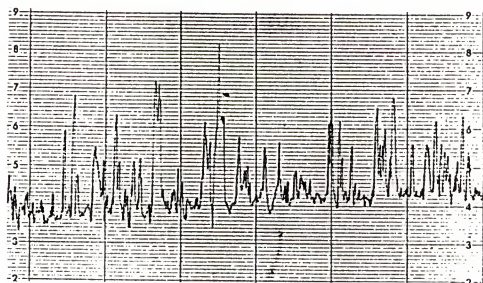


Vertical scale: $1\mu\text{m}/\text{DIV}$ Horizontal scale: $0.1\text{cm}/\text{DIV}$



Vertical scale: $1\mu\text{m}/\text{DIV}$ Horizontal scale: $0.1\text{cm}/\text{DIV}$

Fig. B.3 Recorded surface profiles of Specimen C: a) 0° and b) 90°

a) 0° Vertical scale: $1\mu\text{m}/\text{DIV}$ Horizontal scale: $0.1\text{cm}/\text{DIV}$ b) 90° Vertical scale: $1\mu\text{m}/\text{DIV}$ Horizontal scale: $0.1\text{cm}/\text{DIV}$ Fig. B.4 Recorded surface profiles of Specimen D: a) 0° and b) 90°

BIOGRAPHICAL SKETCH

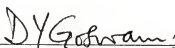
Michael Leung was born in Hong Kong on September 7, 1966. He received his B.S. with honors in mechanical engineering from Oregon State University in 1990 and his M.S. in engineering mechanics from the University of Florida in 1992. He subsequently continued his Ph.D. in the Department of Mechanical Engineering at the University of Florida and was admitted to Ph.D. candidacy in 1994.

I certify that I have read this study and that in my opinion it conforms to acceptable standards of scholarly presentation and is fully adequate, in scope and quality, as a dissertation for the degree of Doctor of Philosophy.



Chung K. Hsieh, Chairman
Professor of Mechanical Engineering

I certify that I have read this study and that in my opinion it conforms to acceptable standards of scholarly presentation and is fully adequate, in scope and quality, as a dissertation for the degree of Doctor of Philosophy.



D. Yogi Goswami, Cochairman
Professor of Mechanical Engineering

I certify that I have read this study and that in my opinion it conforms to acceptable standards of scholarly presentation and is fully adequate, in scope and quality, as a dissertation for the degree of Doctor of Philosophy.



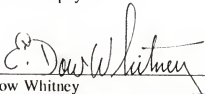
James F. Klausner
Associate Professor of Mechanical
Engineering

I certify that I have read this study and that in my opinion it conforms to acceptable standards of scholarly presentation and is fully adequate, in scope and quality, as a dissertation for the degree of Doctor of Philosophy.



Ulrich H. Kurzweg
Professor of Aerospace Engineering,
Mechanics, and Engineering Science

I certify that I have read this study and that in my opinion it conforms to acceptable standards of scholarly presentation and is fully adequate, in scope and quality, as a dissertation for the degree of Doctor of Philosophy.


E. Dow Whitney
Professor of Materials Science and
Engineering

This dissertation was submitted to the Graduate Faculty of the College of Engineering and to the Graduate School and was accepted as partial fulfillment of the requirements for the degree of Doctor of Philosophy.

August, 1995


for Winfred M. Phillips
Dean, College of Engineering

Karen A. Holbrook
Dean, Graduate School